An investigation of a turbulent spray flame using Large Eddy Simulation with a stochastic breakup model

W. P. Jones, A. J. Marquis, D. Noh[*]

Department of Mechanical Engineering, Imperial College London, Exhibition Road, London SW7 2AZ, UK

Abstract

A computational investigation of a turbulent methanol/air spray flame in which a poly-dispersed droplet distribution is achieved through the use of a pressure-swirl atomiser (also known as a simplex atomiser) is presented. A previously formulated stochastic approach towards the modelling of the breakup of droplets in the context of Large Eddy Simulation (LES) is extended to simulate methanol/air flames arising from simplex atomisers. Such atomisers are frequently used to deliver fine droplet distributions in both industrial and laboratory configurations where they often operate under low-pressure drop conditions. The paper describes improvements to the breakup model that are necessary to correctly represent spray formation from simplex atomisers operated under low-pressure drop conditions. The revised breakup model, when used together with the existing stochastic models for droplet dispersion and evaporation, is shown to yield simulated results for a non-reacting spray that agree well with the experimentally measured droplet distribution, spray dynamics and size-velocity correlation. The sub-grid scale (*sgs*) probability density function (*pdf*) approach in conjunction with the Eulerian stochastic field method are employed to represent the unknown interaction between turbulence and chemistry at the sub-filter level while a comprehensive kinetics model for methanol oxidation with 18 chemical species and 84 elementary steps is used to account for the gas-phase reaction. A qualitative comparison of the simulated OH images to those obtained from planar laser-induced fluorescence (PLIF) confirms that the essential features of this turbulent spray flame are well captured using the *pdf* approach. They include the location of the leading-edge combustion (or lift-off height) and the formation of a double reaction zone due to the polydisperse spray. In addition, the influence of the spray flame on the structure of the reacting spray in respect of the mean droplet diameters and spray velocities is reproduced to a good level of accuracy.

Keywords:
Large Eddy Simulation, Probability Density Function (PDF) approach, Eulerian stochastic field method, Stochastic breakup model, Pressure-swirl atomiser, Droplet evaporation

1. Introduction

In many practical devices ranging from gas turbine aircraft engines, gasoline direct injection engines to liquid propellant rocket motors, turbulent reactive flows with liquid droplets are often encountered. In order to enhance the quality of droplet distributions, the delivery of liquid fuels into combustion chambers is achieved through primary and secondary atomisation. Disintegration of liquid fuel into ligaments (*primary breakup*) can be achieved by various

---

[*]Corresponding author
Email address: dongwon.noh10@imperial.ac.uk (D. Noh)

methods with its driving principles which vary depending on the type of fuel delivery systems [1]. The most commonly used form is a pressure drop within an atomiser which gives rise to an increase in kinetic energy of the liquid that then results in atomisation due to the growth of instability of the liquid jet/sheet mainly caused by its interaction with the surrounding gas. In general, pressure atomisers can be classified into three different types; jet, swirl and jet-swirl atomisers [2]. In pressure-swirl atomisers of interest in this work, typically, a hollow-conical, swirling liquid sheet emerges from the nozzle and spreads outwards radially. The liquid sheet becomes unstable due to aerodynamic forces acting on its surface and experiences fragmentation into ligaments and relatively large drops. They may then experience another stage of fragmentation into even smaller drops; this process is referred to as *secondary breakup*. When disruptive aerodynamic forces are large enough, drops start to deform and eventually break into a multitude of small fragments. The manner in which drops undergo deformation and secondary breakup depending on the magnitude of aerodynamic forces has been extensively studied in [3, 4]. The resulting droplets in the shape of a hollow-cone spray then evaporate and create fuel vapour which mixes with the surrounding gas and burns. The general behaviour of the spray is, in parallel, influenced through its interaction with a turbulent spray flame. This whole process, from the breakup of droplets to the formation of a spray flame, occurs over a wide range of time and length scales. It is thus necessary to employ an accurate and detailed modelling approach if the complex phenomena associated with both phases are to be captured.

Despite ongoing efforts by various researchers, the physics involved in spray formation in pressure-swirl atomisers is not fully understood and its modelling remains difficult. The majority of theoretical works on the primary breakup of a liquid sheet relies on a concept of the aerodynamic perturbations growing on the liquid surface, leading to its disintegration into ligaments and large drops. In addition to this aerodynamic instability theory, experimental works [5, 6] provide important insight into other mechanisms towards liquid sheet disintegration. For example, fragments torn off the liquid sheet quickly contracting into ligaments can be generated due to the formation of perforations on the sheet. Perforated-sheet disintegration is not well understood, but impingement of small drops on the liquid surface, turbulent motions inside the sheet, etc., may be the main factors causing the onset of holes along the surface of liquid sheets. This complexity has led to a general acceptance, at least in modelling perspectives, that aerodynamic instability mainly causes the liquid film to experience disintegration. Following the pioneering work by Squire [7] on the instability of a moving liquid film, many attempts have been made to gain a better understanding of liquid sheet disintegration. In the work of Dombrowski and Johns [8], a dispersion relation for the growth rate of long waves with infinitesimal amplitude was derived through consideration of the effects of aerodynamic forces, surface tension and liquid viscosity. The wavelength for the maximum growth rate was determined and assumed to cause the breakup of liquid sheet into ligaments. Schmidt *et al.* [9, 10] proposed a model for pressure-swirl atomisation which is known as the Linearised Instability Sheet Atomisation (LISA) model. From this linear stability analysis, the sheet breakup length in addition to droplet size distributions can be determined.

The design of spray injection systems leading to a reduction in the final size of the atomised droplets and hence an increase in the evaporation rate is vital if advances in the overall performance of particle-laden combusting flows are to be achieved, with combustion efficiency being improved and pollutant emission rates being controlled. Consequently, researchers have made considerable attempts at investigating the challenging issues involved in turbulent reacting flows laden with liquid droplets. Historically, the atomisation process has been represented by widely accepted breakup models such as the Taylor Analogy Breakup (TAB) [11] and the surface wave instability (WAVE) model of Reitz [12]. The TAB model is based upon Taylor's analogy to represent the oscillation of mother droplets as a spring-mass system whilst the WAVE model employs a linear stability analysis of liquid jets to determine the

growth of Kelvin-Helmholtz waves on the surface of the injected liquid 'blobs'. These breakup models have been widely used in studies of droplet breakup as they can be readily implemented into existing CFD codes.

In the context of Large Eddy Simulation (LES), deterministic breakup models have not gained popularity as they are applicable mainly in Reynolds Averaged Navier-Stokes (RANS) approaches. To the authors' knowledge, there have been few previous efforts devoted to the investigation of liquid atomisation using LES. Apte *et al.* [13] are amongst the few who have introduced stochastic sub-grid models in LES of an atomising spray. Their model is based on Kolmogorov's discrete model which is rewritten in the form of Fokker-Planck equation to determine the probability of the size of daughter droplets. In the present work the stochastic model for the spray atomisation formulated by Jones and Lettieri [14] is adopted and further developed for the modelling of liquid droplets formed by pressure-swirl atomisers. A Monte Carlo trajectory integration is used to represent the influence of gas-phase fluctuating motions on the secondary breakup of droplets. The validity of the breakup model of Jones and Lettieri has been demonstrated by comparisons with the experimental results of Park *et al.* [15] and the measurement of Hiroyasu and Kadota [16]. However, the application of the model has been mainly to non-reacting sprays and there exist only few previous studies in which stochastic breakup models have been applied to atomisation in turbulent two-phase flames [17, 18].

LES has been successfully applied in many complex flows since the conceptual foundations laid in the pioneering works of Smagorinsky [19] and Lilly [20]. For turbulent combustion many different LES models have been proposed including, for example, artificially thickened flames (ATF), Conditional Moment Closure (CMC) and Flame Surface Density (FSD). A comprehensive review of LES combustion models can be found in the paper by Pitsch [21]. In recent years, the probability density function (*pdf*) method, which was originally developed in the context of RANS, has been extended to LES on the basis of a transport equation which describes the temporal evolution of the sub-grid scale (*sgs*) *pdf* of scalar quantities [22]. The conventional method adopted to solve the modelled form of the *sgs-pdf* transport equation is that based on stochastic Lagrangian particles [23]. In this work, however, the Eulerian stochastic field method [24, 25] which was extended to LES in [26] is applied. The LES-*pdf* approach in connection with the stochastic field formulation have provided good results in all combustion regimes including auto-ignition in a hot co-flow [27], piloted flames with extinction [28], stratified swirl burner [29] and gas turbine combustion chamber [30] to cite a few examples.

The Eulerian stochastic field method has already been applied to turbulent two-phase combusting flows; limited examples are swirl combustor [31], spark ignition in a gas turbine combustor [32] and auto-ignition in a vitiated co-flow [33]. In all these cases, however, the inlet droplet size distribution and droplet velocities were determined by a trial and error procedure, an approach which may involve many additional simulations in order to match measured profiles. This paper therefore attempts to formulate an approach for the breakup of liquid droplets and that avoids (or minimises) the need to estimate droplet properties in LES-*pdf* simulations of a turbulent two-phase reactive flow. The stochastic breakup model in conjunction with the transported *sgs-pdf* equation approach are applied to study phenomena such as turbulence-chemistry interaction, droplet dispersion and evaporation and liquid atomisation. The measurements of McDonell *et al.* [34, 35] in a turbulent methanol spray flame arising from a pressure-swirl atomiser are used to confirm the predictive capabilities of the LES methodology.

The turbulent spray flame under consideration in the present work has been the subject of a number of RANS based computational studies. Both flamelet and *pdf* methods have been applied, Hollmann and Gutheil [36], Hollmann and Gutheil [37], Ge and Gutheil [38, 39] and Ge *et al.* [40]. For example, a joint mixture fraction-enthalpy *pdf* was introduced in [39] while an extended $k - \epsilon$ model [37] was employed to close the transported *pdf* equations and to provide mean values of the gas flow required for spray computations. Measurements of droplet properties at the

first cross section were used to specify the initial conditions in all these previous studies and the main cause of the large differences between the predicted results and experimental data was attributed [36] to an insufficient amount of measurements being available. Spray computations are very sensitive to estimated droplet inlet characteristics which means that a detailed set of measurements close to the injection point is needed in the approach adopted by these authors. The use of the droplet breakup model in the present work is aimed at minimising the need for detailed measurements in the vicinity of the injection point. Additionally, as far as the authors are aware, the present investigation appears to represent a first LES effort to characterise the behaviour of the spray flame of interest using a secondary breakup model. The LES results are then examined to provide a better visualisation of the time-dependent interaction between the spray flame and liquid droplets, yielding a deeper insight into the stability mechanism of the flame.

2. Details of mathematical modelling

2.1. LES governing equations with the presence of liquid drops

The fundamental aspect of LES is the use of a spatial filter to separate the resolved, large-scale energy-containing motions from those with scales smaller than the size of the filter width. In order to achieve scale separation in the required LES governing equations, a low-pass filter is applied to the conservation equations of mass, momentum and relevant scalars such as species mass fractions and enthalpy. Consequently, the large-scale energetic turbulent motions can be explicitly solved for whereas the influence of the unresolved motions on the resolved turbulence must be accounted for via appropriate sub-grid modelling. In turbulent reacting flows where large variations of the fluid density are present, the most straightforward way of accounting for these fluctuations is to apply a density-weighted (or Favre-weighted) filtering [41]. The density-weighted filtered governing equations of the low-Mach number, variable density flow, with the influence of the dispersed phase included, can be written as:

$$\frac{\partial \bar{\rho}_g}{\partial t} + \frac{\partial \left(\bar{\rho}_g \tilde{u}_j \right)}{\partial x_j} = \bar{\dot{m}} \tag{1}$$

$$\frac{\partial \left(\bar{\rho}_g \tilde{u}_j \right)}{\partial t} + \frac{\partial \left(\bar{\rho}_g \tilde{u}_i \tilde{u}_j \right)}{\partial x_j} = -\frac{\partial \bar{p}}{\partial x_i} + \frac{\partial \bar{\tau}_{ij}}{\partial x_j}$$
$$- \frac{\partial \tilde{\tau}_{ij}^{sgs}}{\partial x_j} + \bar{\rho}_g g_i + \bar{f}_{mom,i} \tag{2}$$

$$\frac{\partial \left(\bar{\rho}_g \tilde{\phi}_\alpha \right)}{\partial t} + \frac{\partial \left(\bar{\rho}_g \tilde{\phi}_\alpha \tilde{u}_j \right)}{\partial x_j} = \frac{\partial}{\partial x_j} \left(\frac{\mu}{\sigma} \frac{\partial \tilde{\phi}_\alpha}{\partial x_j} \right) - \frac{\partial \tilde{J}_{j,\alpha}^{sgs}}{\partial x_j}$$
$$+ \overline{\rho_g \dot{\omega}_\alpha \left(\underline{\phi}, T \right)} + \bar{\dot{m}}_\alpha \qquad 1 \leq \alpha \leq N_s \tag{3}$$

where $\bar{\rho}_g$ is the density of the gaseous mixture, $\tilde{u}_i$ is the gas velocity in the i-th direction, $\bar{p}$ is the static pressure, μ is the dynamic viscosity of the fluid and g_i is the gravitational acceleration. N_s is the number of scalar quantities, *ie* the number of chemical species plus one. The quantities, $\bar{\tau}_{ij}$ and $\tilde{\tau}_{ij}^{sgs}$, appearing in Eq. (2) are the viscous part of the resolved stress tensor and the residual stress tensor, respectively. To close the latter, defined as $\tilde{\tau}_{ij}^{sgs} = \left(\overline{\rho_g u_i u_j} - \bar{\rho}_g \tilde{u}_i \tilde{u}_j \right)$, a dynamically calibrated version of the Smagorinsky model [42] is adopted in the present work. For the filtered scalar quantities, Eq. (3), such as species mass fractions, Y_α, and the specific enthalpy of the mixture, h, a Lewis number of unity is assumed so that σ is the Schmidt or Prandtl number with a value of 0.7 as appropriate. In Eq. (3) the unknown

4

sub-grid scale scalar flux is given by $\tilde{J}_{j,\alpha}^{sgs} = \left(\overline{\rho_g \phi_\alpha u_j} - \bar{\rho}_g \tilde{\phi}_\alpha \tilde{u}_j\right)$ and the chemical source term, $\dot{\omega}_\alpha\left(\underline{\phi}, T\right)$, represents the net rate of formation and consumption of the reactive species through chemical reaction. The accurate evaluation of the reaction rates is the major challenge in the modelling of turbulent reacting flows due to the presence of a strong coupling between turbulence and chemistry; the influence of sub-grid scale fluctuations on chemical reaction cannot be ignored. The chemical reaction term cannot be determined using only the filtered mean quantities and thus necessitates a suitable closure which will be explained in the following subsection. Equation (3) is not solved directly, but rather the evolution of the scalar fields is described in terms of the appropriate *pdf*. The filter width, Δ, is taken to be the cubic root of the volume of the local grid cell. Lastly, the phase exchange source terms of mass, momentum and relevant scalars, *ie* $\bar{\dot{m}}$, $\bar{f}_{mom,i}$ and $\bar{\dot{m}}_\alpha$ respectively, are obtained from a summation of the effects of every p-th particle instantaneously located in a specific filter volume, *e.g.* $\bar{\dot{m}} = -\frac{1}{\Delta^3} \sum_{p=1}^{N_p} \dot{m}_p$.

2.2. LES-PDF formulation: Eulerian stochastic field method

The generic transport equation for scalars, *ie* Eq. (3), contains the chemical source term which is highly nonlinear and requires careful treatment. In the present work, a detailed description of the unknown interaction between sub-grid scale turbulent motions and chemical reaction is achieved through the introduction of the one-time, one-point joint sub-grid scale *pdf*. With the use of the filtering operation and the sifting property of the Dirac delta function, an exact equation (see Gao and O'Brien [22]) governing the temporal evolution of the density-weighted *sgs-pdf* for the N_s scalars, *ie* mass fraction of the N_α chemical species and specific enthalpy of the gaseous mixture ($N_s = N_\alpha + 1$), can be written as:

$$
\begin{aligned}
&\bar{\rho}\frac{\partial \tilde{P}_{sgs}\left(\underline{\psi}\right)}{\partial t} + \bar{\rho}\tilde{u}_j \frac{\partial \tilde{P}_{sgs}\left(\underline{\psi}\right)}{\partial x_j} - \frac{\partial}{\partial x_i}\left(\frac{\mu}{\sigma}\frac{\partial \tilde{P}_{sgs}\left(\underline{\psi}\right)}{\partial x_i}\right) + \sum_{\alpha=1}^{N_s} \frac{\partial}{\partial \psi_\alpha}\left[\bar{\rho}\dot{\omega}_\alpha(\underline{\psi})\tilde{P}_{sgs}\left(\underline{\psi}\right)\right] \\
&+ \sum_{\alpha=1}^{N_s} \frac{\partial}{\partial \psi_\alpha}\left[\frac{\bar{\rho}\left(\dot{m}_\alpha(\underline{\psi}) - \dot{m}(\underline{\psi})\psi_\alpha\right)}{\rho(\underline{\psi})}\tilde{P}_{sgs}(\underline{\psi})\right] = -\frac{\partial\left(\overline{\rho u_j \mathcal{F}(\underline{\psi})} - \bar{\rho}\tilde{u}_j\tilde{P}_{sgs}(\underline{\psi})\right)}{\partial x_j} \\
&- \sum_{\alpha=1}^{N_s}\sum_{\beta=1}^{N_s} \frac{\partial^2}{\partial \psi_\alpha \partial \psi_\beta}\left[\left(\frac{\mu}{\sigma}\overline{\frac{\partial \phi_\alpha}{\partial x_i}\frac{\partial \phi_\beta}{\partial x_i}\bigg|\underline{\phi}=\underline{\psi}}\right)\tilde{P}_{sgs}\left(\underline{\psi}\right)\right]
\end{aligned}
\tag{4}
$$

where $\mathcal{F}(\underline{\psi})$ is the fine-grained *pdf* and the terms, $\dot{m}_\alpha$ and $\dot{m}$, represent the rate per unit volume at which mass of the species α and mass of the mixture, through the evaporation of liquid droplets, are added to the continuous phase. All the terms including the chemical reaction term on the left hand side of Eq. (4) appear in a closed form; this is the main advantage of the *pdf* approach for studying turbulent reacting flows as no further closure method is required by the inclusion of chemical reaction. In contrast, there are two well-known unknown terms which appear on the right hand side of Eq. (4), representing the *sgs* transport of the joint *pdf* (first term) and the unknown influence of the molecular mixing at scales smaller than the size of the filter width (second term). These two processes require modelling as all information below the sub-filter level is lost in the LES approach. In the present work, the *sgs* transport of the *pdf* is accounted for by the Smagorinsky type gradient model:

$$
\left(\overline{\rho u_j \mathcal{F}(\underline{\psi})} - \bar{\rho}\tilde{u}_j\tilde{P}(\underline{\psi})\right) = -\frac{\mu_{sgs}}{\sigma_{sgs}}\frac{\partial \tilde{P}_{sgs}(\underline{\psi})}{\partial x_j}
\tag{5}
$$

where μ_{sgs} is the sub-grid viscosity given by the dynamic Smagorinsky model and σ_{sgs} is the sub-grid Schmidt number assigned a value of 0.7 [26, 33]. In order to close the micro-mixing term, a simple model known as the Linear Mean

Square Estimation (LMSE) [43] or the interaction by exchange with the mean (IEM) [44] is adopted. This approach is formulated based on the fact that there is a reduction in scalar fluctuations due to the molecular mixing. Applying these two closure models to Eq. (4), the transport equation for the joint *sgs-pdf* of scalar quantities can be expressed in the following modelled form:

$$
\begin{aligned}
&\bar{\rho}\frac{\partial \tilde{P}_{sgs}\left(\underline{\psi}\right)}{\partial t} + \bar{\rho}\tilde{u}_j\frac{\partial \tilde{P}_{sgs}\left(\underline{\psi}\right)}{\partial x_j} + \sum_{\alpha=1}^{N_s}\frac{\partial}{\partial \psi_\alpha}\left[\bar{\rho}\dot{\omega}_\alpha(\underline{\psi})\tilde{P}_{sgs}\left(\underline{\psi}\right)\right] \\
&+ \sum_{\alpha=1}^{N_s}\frac{\partial}{\partial \psi_\alpha}\left[\frac{\bar{\rho}\left(\dot{m}_\alpha(\underline{\psi}) - \dot{m}(\underline{\psi})\psi_\alpha\right)}{\rho(\underline{\psi})}\tilde{P}_{sgs}(\underline{\psi})\right] = \frac{\partial}{\partial x_i}\left[\left(\frac{\mu}{\sigma} + \frac{\mu_{sgs}}{\sigma_{sgs}}\right)\frac{\partial \tilde{P}_{sgs}\left(\underline{\psi}\right)}{\partial x_i}\right] \\
&- \frac{C_d}{\tau_{sgs}}\sum_{\alpha=1}^{N_s}\frac{\partial}{\partial \psi_\alpha}\left[\bar{\rho}\left(\psi_\alpha - \tilde{\phi}_\alpha\left(\boldsymbol{x},t\right)\right)\tilde{P}_{sgs}\left(\underline{\psi}\right)\right]
\end{aligned}
\tag{6}
$$

where the micro-mixing time scale τ_{sgs} is defined as $\frac{\bar{\rho}\Delta^2}{\mu+\mu_{sgs}}\left(1 - \exp(-\mathcal{R}^2)\right)$, where $\mathcal{R}$ is defined as the ratio of sub-grid to molecular viscosity, and C_d is the micro-mixing constant with a value of 2.0 [33, 45].

The closed form of the *sgs-pdf* evolution equation, Eq. (6), is solved using the Eulerian stochastic field method based on an Ito interpretation of the stochastic integral. The temporal evolution of the joint *sgs-pdf* is represented by an ensemble of N stochastic fields with each field involving the N_s scalars, namely $\xi_\alpha^n(\boldsymbol{x},t)$ with $1 \leq n \leq N$ and $1 \leq \alpha \leq N_s$. These fields evolve according to:

$$
\begin{aligned}
\bar{\rho}d\xi_\alpha^n = &-\bar{\rho}\tilde{u}_i\frac{\partial \xi_\alpha^n}{\partial x_i}dt + \frac{\partial}{\partial x_i}\left(\Gamma'\frac{\partial \xi_\alpha^n}{\partial x_i}\right)dt \\
&+ \bar{\rho}\sqrt{\frac{2\Gamma'}{\bar{\rho}}}\frac{\partial \xi_\alpha^n}{\partial x_i}dW_i^n - \bar{\rho}\frac{C_d}{2\tau_{sgs}}\left(\xi_\alpha^n - \tilde{\phi}_\alpha\right)dt \\
&+ \bar{\rho}\dot{\omega}_\alpha^n(\underline{\xi}^n)dt + \left(\dot{m}_\alpha(\tilde{\phi}_\alpha) - \dot{m}(\tilde{\phi}_\alpha)\xi_\alpha^n\right)dt
\end{aligned}
\tag{7}
$$

where dW_i^n is an increment of the Wiener process, different for each spatial direction i and each stochastic field n, but independent of the spatial location $\boldsymbol{x}$. The Wiener process is represented as $dW_i^n = \xi_i^n\sqrt{\Delta t}$, where ξ_i^n is a $\{-1, +1\}$ dichotomous random variable. The stochastic term has no influence on the first moments (*ie* filtered mean values) of ξ_α^n. The solution of Eq. (7) for each field satisfies the mass conservation and preserves the boundedness of the scalar of interest because the gradient of the scalar tends to zero when approaching extrema (*e.g.* the species mass fraction is always positive and sums to unity). The filtered mean values of each scalar $\tilde{\phi}_\alpha$ can be evaluated by the following ensemble average over the stochastic fields:

$$
\tilde{\phi}_\alpha = \frac{1}{N}\sum_{n=1}^{N}\xi_\alpha^n
\tag{8}
$$

The liquid-phase contribution in Eq. (7) is evaluated via the spray equations, which will be described in the following subsections, on the basis of the filtered mean continuous phase values of species concentrations and enthalpy. The role of the micro-mixing term is to drive instantaneous chemical compositions or enthalpy of the n-th stochastic field towards their ensemble-averaged value according to the sub-grid time scale. These N stochastic fields constitute a set of stochastic realisations, which are statistically equivalent to the one-point *sgs-pdf* equation [46]. Each field is smooth on the scale of the filter width and should not be confused with any particular realisation of the real flow field.

2.3. PDF modelling of Lagrangian droplets

Following the work of Bini and Jones [47], the probabilistic representation of the dispersed phase is adopted to describe the physical state of a single droplet at time t in terms of a set of macroscopic variables including its velocity V, its diameter D and its temperature Θ. In order to account for droplet breakup, additionally, the droplet number N is introduced as a stochastic variable. The required filtered joint *pdf*, denoted by $\bar{P}_{spr}(v, d, \theta, n; x, t)$ where $\Psi = \{v, d, \theta, n\}$ is the corresponding phase space for the state vector $\Phi = \{V, D, \Theta, N\}$, evolves according to the following exact form of the partial differential equation:

$$\frac{\partial \bar{P}_{spr}}{\partial t} + \frac{\partial(a\bar{P}_{spr})}{\partial v} + \frac{\partial(\dot{\mathcal{D}}\bar{P}_{spr})}{\partial d} + \frac{\partial(\dot{\mathcal{T}}\bar{P}_{spr})}{\partial \theta} + \frac{\partial(\dot{\mathcal{N}}\bar{P}_{spr})}{\partial n} = 0 \tag{9}$$

where a is the conditional droplet acceleration, $\dot{\mathcal{D}}$ is the conditional rate of change of droplet diameter through evaporation, $\dot{\mathcal{T}}$ is the conditional rate of change of droplet temperature caused by heat transfer between the surrounding gas and droplets and $\dot{\mathcal{N}}$ is the conditional rate of change of droplet number through droplet breakup process; these quantities can be expressed in the general form as follows:

$$E\left(\frac{D\psi_k}{Dt} | \Phi = \Psi\right) \quad \text{where} \quad \Psi = v, d, \theta \text{ and } n \tag{10}$$

where $E\left(\frac{D\psi_k}{Dt} | \Phi = \Psi\right)$ is the expectation of $\frac{D\psi_k}{Dt}$ conditioned upon $\Phi = \Psi$ anywhere within the filter volume. Since these quantities are unknown, models are required in order to close Eq. (9). In order to solve the modelled version of Eq. (9), it is replaced with an equivalent Ito system [46] of stochastic differential equations describing the trajectories of stochastic droplets in the phase space $\{v, d, \theta, n\}$. The unclosed terms appearing in Eq. (9) are decomposed into a deterministic part and a stochastic contribution. The deterministic contribution to the Lagrangian rates of change of the relevant variables is evaluated using only the filtered values of the gas-phase properties at the droplet location whereas the additional influence of the unresolved fluctuations on the filtered Lagrangian rates of change requires a modelling procedure.

2.3.1. Droplet dispersion: acceleration

The deterministic contribution to the particle acceleration consists of only viscous drag and gravitational forces taken from the Maxey and Riley formulation [48] while a stochastic Markov model of Bini and Jones [49, 47] is adopted to determine the unknown effects of the unresolved velocity fluctuations of the carrier flow on the dispersion of droplets. The dispersion of the p-th stochastic particle over a time interval dt is given by:

$$d\boldsymbol{u}_p = \frac{\tilde{\boldsymbol{u}} - \boldsymbol{u}_p}{\tau_p} dt + \sqrt{C_o \frac{k_{sgs}}{\tau_t}} d\boldsymbol{W}_t + \left(1 - \frac{\bar{\rho}_g}{\rho_l}\right) \boldsymbol{g} \, dt \tag{11}$$

where $\boldsymbol{u}_p$ is the velocity of the p-th particle, $\tilde{\boldsymbol{u}}$ and $\bar{\rho}_g$ are the filtered gas velocity and density interpolated at the particle position, C_o is a model constant assigned a value of unity [50, 33], k_{sgs} is the unresolved kinetic energy of the gas-phase, $d\boldsymbol{W}_t$ is the increment of the Wiener process, ρ_l is the liquid density and $\boldsymbol{g}$ is the gravitational acceleration. The sub-grid time scale τ_t which determines the rate of interaction between stochastic particles and small-scale turbulence in the gas-phase is given by:

$$\tau_t = \frac{\tau_p^{2\alpha}}{\left(\frac{\Delta}{k_{sgs}^{1/2}}\right)^{2\alpha-1}} \tag{12}$$

where the parameter $\alpha = 0.8$ is used as specified in [49] in order to reproduce the experimentally observed heavy tailed *pdf*s and high levels of probability of extreme acceleration events. The *sgs* kinetic energy of the gas-phase is calculated from $k_{sgs} = (2\Delta \tilde{S}_{ij} \tilde{S}_{ij})^{2/3}$ where $\tilde{S}_{ij}$ is the resolved strain rate tensor, an expression derived from an equilibrium assumption. The particle response time τ_p is defined as:

$$\tau_p = \frac{4}{3} \frac{\rho_l D_p}{\bar{\rho}_g C_D} \frac{1}{|\tilde{u} - u_p|} \tag{13}$$

where D_p is the diameter of the p-th particle and C_D is the particle drag coefficient which is determined from the draw law of Yuen and Chen [51]:

$$C_D = \begin{cases} \frac{24}{Re}\left(1 + \frac{Re^{2/3}}{6}\right) & : 0 < Re < 1000 \\ 0.424 & : Re \geq 1000 \end{cases} \tag{14}$$

where Re is the Reynolds number based on the droplet diameter and the relative velocity of the droplet with respect to the surrounding gas flow. In order to further consider the influence of droplet deformation on the drag coefficient, a simple correlation [52] is adopted in this work. In this dynamic drag model, the effective drag coefficient of deformed drops is assumed to linearly vary between that of a sphere and a flat disk.

2.3.2. Droplet evaporation

The evaporation model of Abramzon and Sirignano [53] adopted in this work is an extended version of the infinite conductivity model in which account is taken of such important effects as variable thermophysical properties, the influence of Stefan flow on heat and mass transfer and non-unitary Lewis number in the gas film. In their revised model, the corrected heat transfer number B'_T is determined through the modified values of Nusselt and Sherwood numbers Nu^* and Sh^*:

$$B'_T = (1 + B_M)^\phi - 1, \quad \phi = \frac{C_{p,v}}{C_{p,g}} \frac{Sh^*}{Nu^*} \frac{1}{Le} \tag{15}$$

$$Nu^* = 2 + \frac{Nu_0 - 2}{F_T} \tag{16}$$

$$Sh^* = 2 + \frac{Sh_0 - 2}{F_M} \tag{17}$$

where $C_{p,v}$ and $C_{p,g}$ are the fuel vapour and gas specific heat capacities at constant pressure, Le is the Lewis number and the correction factors, F_T and F_M, are given by:

$$F_T = \frac{(1 + B'_T)^{0.7}}{B'_T} \ln(1 + B'_T) \tag{18}$$

$$F_M = \frac{(1 + B_M)^{0.7}}{B_M} \ln(1 + B_M) \tag{19}$$

in which $B_M = \frac{Y_{F,s} - Y_{F,\infty}}{1 - Y_{F,s}}$, where $Y_{F,s}$ represents the mass fraction of the droplet vapour at its surface and $Y_{F,\infty}$ refers to the free stream vapour mass fraction away from the droplet surface, is the Spalding transfer number. It should be noted that the Ranz-Marshall correlations for Nu and Sh [54, 55] over-predict the mass and heat transfer rates at low Reynolds numbers, $Re \leq 10$. Abramzon and Sirignano [53] pointed out that they may lead to the physically incorrect super sensitivity of the transfer rates to the small turbulent velocity fluctuations in the vicinity of zero Reynolds number because of $(dNu/dRe)_{Re\to 0} = \infty$. Furthermore, Crocco [56] noted that this could result in erroneous

simulations during a combustion instability analysis. The following equations by Clift *et al.* [57] can be used as an alternative to the Ranz-Marshall correlations:

$$Nu_0 = 1 + (1 + RePr_g)^{1/3} f(Re) \tag{20}$$

$$Sh_0 = 1 + (1 + ReSc_g)^{1/3} f(Re) \tag{21}$$

in which Pr_g and Sc_g are the gas-phase Prandtl and Schmidt numbers and $f(Re)$ is given by:

$$f(Re) = \begin{cases} Re^{0.077} & : 1 < Re \leq 400 \\ 1 & : Re \leq 1 \end{cases} \tag{22}$$

The above expressions are valid up to Reynolds numbers of 400 and the typical range of Re in the experimental configuration of interest falls within the range. This evaporation model involves an iterative procedure for the determination of B'_T which may result in an increase in the computational cost that may be expensive for spray calculations with very large numbers of droplets. However, as found by others [58, 53] and confirmed in the present work the transfer number reaches a converged value typically within two or three iterations. Chen and Periera [59] conducted many-droplet spray calculations with the rapid mixing model and the Abramzon-Sirignano model and concluded that the latter model gave improved agreement with measurements. With a knowledge of both B'_T and Sh^*, the rates of change of temperature T_p and mass m_p of the p-th droplet can now be obtained from the following expressions:

$$\frac{dT_p}{dt} = -\frac{\dot{m}_p}{m_p B'_T} \left(\frac{C_{p,v}}{C_{p,l}} \right) (T_g - T_p) + \left(\frac{h_{fg}}{C_{p,l}} \right) \frac{\dot{m}_p}{m_p} \tag{23}$$

$$\dot{m}_p = \frac{dm_p}{dt} = -\frac{Sh^*}{3Sc_g} \left(\frac{m_p}{\tau_p} \right) H_M \tag{24}$$

where $C_{p,l}$ is the specific heat capacity of the liquid, T_g is the interpolated gas-phase temperature at the droplet position, h_{fg} is the latent heat of vaporisation and $H_M = \ln(1 + B_M)$ is the mass transfer potential.

Following the method proposed in the work of Bini and Jones [50], the influence of the missing sub-grid velocity fluctuations on the temporal evolution of droplet mass is taken into account by decomposing the parameter governing convection (*ie* Sherwood number) into two parts: the resolved contribution Sh^{dt} and the unresolved part Sh^{sgs}. The rate of change of droplet mass after this decomposition can be expressed in the following manner:

$$dm_p = -\frac{m_p}{3Sc_g\tau_p} \left(Sh^{dt} + Sh^{sgs} \right) \ln(1 + B_M) dt \tag{25}$$

where the deterministic Sherwood number is calculated by Eq. (17) while the stochastic contribution to Eq. (25) is defined as:

$$Sh^{sgs}dt = C_v Sc_g^{1/3} \left(\bar{\rho}_g \frac{k_{sgs}^{1/2} D_p}{\mu_g} \right)^{1/2} |dW_t|^{1/2} \tau_p^{3/4} \tag{26}$$

where C_v is a model constant with a value of unity as applied in [50, 33]. A similar term to the Nusselt number could be introduced, but was not considered herein because the influence of Sh^{sgs} on the evaporation rate was found to be small in comparison to Sh^{dt}.

For any given evaporation model, the values of droplet vaporisation rate are found to be very sensitive to the

choice of thermophysical properties [60]. All the gas-phase properties with the subscript $(\cdot)_g$ in Eqs. (15) - (26) relate to the properties of a mixture comprising the liquid vapour and the surrounding gas. The most common approach to evaluating the mixture properties is to use an interpolation between the droplet surface, s, and the far-field, ∞, weighted with a factor of 1/3, Hubbard *et al.* [61]. According to this simple rule, the reference states in terms of the temperature (T_{ref}) and mass fraction (Y_{ref}) are defined as:

$$T_{ref} = T_s + 1/3 \left(T_\infty - T_s\right) \qquad Y_{ref} = Y_s + 1/3 \left(Y_\infty - Y_s\right) \tag{27}$$

from which all the necessary properties of the mixture are calculated. The mixture density is evaluated assuming an ideal gas mixture while the specific heat capacities and enthalpy are obtained from JANAF polynomial database [62]. The pure species gas transport properties are calculated from the method of Chung *et al.* [63, 64] for both viscosity and thermal conductivity and the Chapman-Enskog kinetic theory of gases [65] for binary diffusion coefficient. The Wilke mixture rule is used for viscosity [66] and diffusion coefficient [67] and the mixing rule of Wassiljewa [68] is adopted for thermal conductivity.

2.4. Stochastic model for droplet breakup

In this work, an improved version of the stochastic breakup model of Jones and Lettieri [14] is proposed to characterise spray atomisation processes in relation to the use of pressure-swirl atomisers that are operated under low-pressure conditions. The modification of the previous formulation was necessary as its application in the present case led to the production of an excessive number of droplets. The original breakup model was introduced to represent droplet formation in solid-cone liquid jets with high initial velocities typically of order 100 m/s. In this situation Weber numbers are much higher than is the case in the present work. The droplet breakup frequency given by the original model was so high that a vast number of drops were produced and thus no valuable results could be obtained. To overcome this improvements are made in terms of the breakup frequency, the *pdf* of daughter droplet sizes and the expected droplet life time. These are described in the following paragraphs.

The conditional Lagrangian rate of change of droplet number through droplet fragmentation, $\dot{\mathcal{N}}$, which appears in Eq. (9) is represented in a statistical manner. A Monte-Carlo trajectory integration is adopted to compute the effects of both the deterministic contribution and the modelled velocity fluctuations at the sub-filter level on the breakup of droplets. Fragmentation of each droplet is described as a discrete Poisson process while a statistical model for the *pdf* of daughter droplet diameters depending on the turbulent nature of the carrier flow is adopted to determine the size of daughter drops upon each breakup event. As suggested in the work of Lasheras *et al*. [69], the rate at which the number density of droplets changes only due to their fragmentation into smaller ones can be expressed as:

$$\dot{\mathcal{N}} = \int_D^\infty m\left(D_0\right) f\left(D, D_0\right) \omega\left(\epsilon, D_0\right) n\left(D_0, t\right) dD_0 - \omega\left(\epsilon, D\right) n\left(D, t\right) \tag{28}$$

where $m\left(D_0\right)$ is the mean number of droplets resulting from the breakup of a mother droplet of size D_0, $f\left(D, D_0\right)$ is the size distribution of daughter droplets formed from the fragmentation of a mother droplet of size D_0, $\omega\left(\epsilon, D_0\right)$ is the frequency at which droplets of size D_0 experience fragmentation and $n\left(D_0, t\right)$ is the probable number of droplets with size in the range dD about D_0 at time t. The physical interpretation of Eq. (28) is the sum of the birth rate of droplets of size D produced upon the breakage of droplets of sizes larger than D and the death rate of droplets of size D due to their further disintegration into smaller drops. In order to solve Eq. (28), it is necessary to provide appropriate models that are responsible for the modelling of the breakup frequency $\omega\left(\epsilon, D\right)$, the *pdf* of daughter droplet sizes $f\left(D, D_0\right)$

and the expected number of daughter droplets $m(D_0)$. These fragmentation parameters are treated individually as follows.

The present breakup model used to compute the total breakup frequency ω consists of a deterministic contribution mainly due to disruptive aerodynamic forces imposed on droplets by the surrounding gas and a stochastic formulation which is a function of both the dissipation rate of turbulent kinetic energy ϵ and the diameter of mother droplet D:

$$\omega(\epsilon, D) = \frac{1}{\pi} \sqrt{\frac{8\sigma}{\rho_l (D/2)^3}} + K_g \frac{\sqrt{\beta(\epsilon D)^{2/3} - 12\sigma/(\rho D)}}{D} \tag{29}$$

where σ is the surface tension of liquid and β is an integration constant which is assigned a value of 8.2 [70]. The simplex atomiser under investigation is operated at low pressure and therefore the deterministic component of the breakup frequency, *ie* the first term on the right hand side of Eq. (29), is taken as an inverse function of the breakup time [11] for droplets experiencing fragmentation at the Weber number (We) close to its critical value of around 12. This Weber number corresponds to the transition We from vibrational to bag breakup [3]. Typical values of We in the experimental configuration under consideration are found to be in close proximity to the critical value. Based on the experimental work of Martínez-Bazán *et al.* [71] investigating the fragmentation of air bubbles in a turbulent air flow, the stochastic contribution to the total breakup frequency contains the rate of dissipation of kinetic energy which necessitates a reliable knowledge of the variable. In LES, it can be obtained from the following relation, $\epsilon = 2\left(v + v_{sgs}\right)\tilde{S}_{ij}\tilde{S}_{ij}$. The empirical constant, K_g, which is the only fitting parameter in the current stochastic breakup model, was originally determined to be 0.25 by considering the breakup of air bubbles immersed in a water jet. This phenomenological model was further extended to study liquid-liquid systems by Eastwood *et al.* [72]. Lasheras and others [73, 74] also adopted the model to characterise the far-field breakup of a liquid jet by a high-speed annular gas jet. In their investigations, the critical distance, *ie* the distance downstream from the nozzle where a local equilibrium is reached and the turbulent breakup no longer occurs, was measured over a wide range of gas velocities and liquid mass loadings. The measured location of the droplet breakup equilibrium point was found to agree well with the droplet breakup time proposed in [71]. These previous works provide some justification for its application to the breakup of liquid droplets in an air jet. After initial parametric studies in the present investigation, the model constant was assigned a value of 0.10 which was found to result in good agreement with measurements in the vicinity of the injector.

Martínez-Bazán *et al.* [75] also proposed a statistical model to determine the probability density function of the size of daughter particles resulting from the breakup of a mother particle. The model assumes a mechanism of binary droplet breakup leading to daughter droplet diameters, D_1 and $D_2 = D_0 \left[1 - (D_1/D_0)^3\right]^{1/3}$, when a mother droplet with its size of D_0 breaks. However, Martínez-Bazán *et al.* [76] reviewed the model for the daughter size *pdf* and suggested the following corrected version, which satisfies the volume-conserving condition:

$$f^*(D^*) = \frac{D^{*2}\left[D^{*2/3} - \Lambda^{5/3}\right]\left[\left(1 - D^{*3}\right)^{2/9} - \Lambda^{5/3}\right]}{\int_{D^*_{min}}^{D^*_{max}} D^{*2}\left[D^{*2/3} - \Lambda^{5/3}\right]\left[\left(1 - D^{*3}\right)^{2/9} - \Lambda^{5/3}\right] dD^*} \tag{30}$$

where $D^* = D_1/D_0$ and $\Lambda = D_c/D_0$. The critical diameter, $D_c = \left[12\sigma/(\beta\rho)\right]^{3/5}\epsilon^{-2/5}$, simply represents the diameter of the largest droplet which will not undergo any fragmentation under the turbulent action of the flow. The inverse

transform sampling method is adopted to generate random droplet diameters from the *pdf* given by Eq. (30).

The Lagrangian treatment of Eq. (9) governing droplet fragmentation should be made in such a manner that its computational effect remains affordable in the context of LES. In a trajectory point of view, daughter droplets generated upon breakup events should, in principle, follow their own new, independent trajectories in the phase space; this requires that fragmentation needs to be considered as a continuous process. Since this approach would be computationally prohibitive, a discrete Poisson release process [14] is used in order for the breakup process to be modelled at discrete time instants evolving along with the global time step of the gas-phase. The global number of stochastic droplets of size D experiencing fragmentation within the discrete time interval $[t_0, t]$ is therefore represented by the following integration:

$$N_{broken}(D) = \int_{t_0}^{t} \omega(\epsilon, D) N_t(D) dt \tag{31}$$

where $N_t(D)$ is the number of droplets of size D at the instant t. A mother droplet with its initial age of zero is assumed to undergo disintegration into smaller fragments if its characteristic diameter D is greater than the critical diameter D_c and its accumulated age t_{age} is larger than its expected lifetime $t_{break} \equiv 1/\omega$. A Poisson distribution with its mean equivalent to the computed fragmentation frequency of each droplet is used to select random deviates in the droplet lifetime.

Upon each breakup event, two daughter droplets with their sizes determined by Eq. (30) and their physical properties identical to their mother droplet are formed and the parent drop is destroyed. These newly formed droplets, which conserve mass, may subsequently experience another stage of fragmentation into smaller ones. This breakup process is cascading in nature and will persist until the final daughter droplets become stable (*ie* $D < D_c$). The probable change in the total number of stochastic droplets due to the breakup of droplets of diameter $D_0 > D$ or the expected number of daughter droplets resulting from the breakup of droplets $m(D_0)$ is simply the sum of newly formed droplets at each time instant.

3. Numerical setup

3.1. Experimental configuration

The experimental burner investigated here is a turbulent methanol/air spray flame designed at the University of California, Irvine Combustion Laboratory [34, 35]. A type of pressure-swirl atomisers, Research Simplex Atomiser (RSA), manufactured by Parker Hannifin is used to deliver a dilute methanol spray into an air passage. A schematic representation of the experimental apparatus together with a detailed description of the simplex atomiser are shown in Fig. 1. There are three different operating modes through the air passage such as simplex (no atomising air), non-swirling air-assist and swirling air-assist; detailed information on the operating conditions can be found in [77]. The second mode under consideration is a good candidate for the present study of stochastic breakup model since measurements are available for the following three cases:

(i)   *isothermal case without spray* where the choice of the computational setup can easily be assessed.

(ii)   *non-reacting spray case* which does not possess the strong interaction between droplets and the flame meaning that a more complete validation can be made only in terms of the present breakup model.

(iii)   *reacting spray case* where the effects of the flame on the behaviour of droplets can be analysed and the applicability of the Eulerian stochastic field method can be confirmed for this particular spray flame.
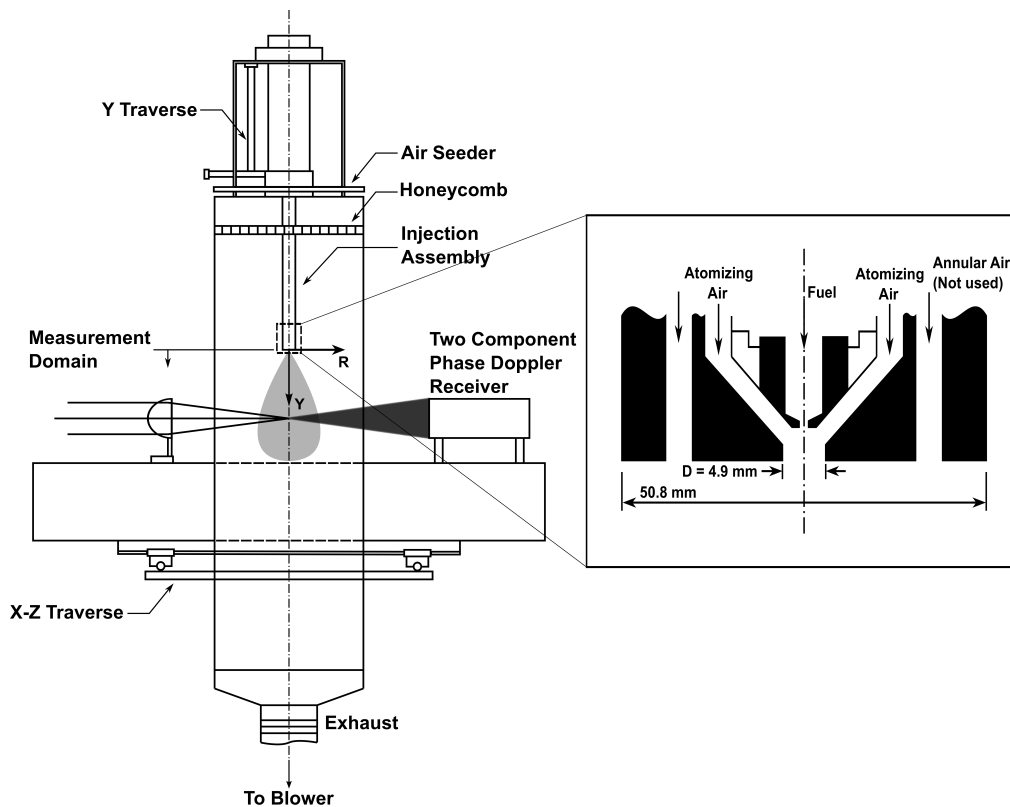
Figure 1: A simple diagram of the experimental configuration under investigation (left) and a detailed representation of the simplex injector tip and the air passage within the injection assembly (right). Please note that drawing is not to scale.

The simplex injector tip which is mounted centrally within the air passage produces a hollow-cone annular sheet with a nominal full spray angle of 85°. The methanol fuel is delivered at a mass flow rate of 1.26 g/s corresponding to a pressure drop of 420 kPa while the atomising air through the air passage is injected at a mass flow rate of 1.32 g/s (3.48 and 3.73 kPa pressure drop for conditions in the absence and presence of spray respectively). The fuel injector assembly comprising a flat end and an exit of 4.9 mm in diameter (D = 4.9 mm) is placed at the centre of a 495 × 495 mm square duct. Methanol and air are injected at room temperatures ranged between 18 and 22 °C. This operating condition corresponds to a Reynolds number of 20,000 based on the diameter of the injection assembly exit D and a bulk velocity of 62.5 m/s through the atomiser opening. Additional air which surrounds the injection assembly is introduced through the top of the duct by a blower and has an average velocity of 1.0 m/s. A lifted flame with its base situated between 50 and 60 mm away from the atomiser exit arises and the flame blows off at higher Reynolds numbers starting from 22,640.

The gas velocity statistics both without and with liquid spray were measured with Phase Doppler-Interferometry (PDI) by the use of 2 μm alumina power in order to seed the carrier flow. The PDI system was also applied to measure other quantities including liquid volume flux, droplet size and droplet velocity as a function of size classes. In addition, infrared extinction/scattering (IRES) was utilised to obtain measurements for the fuel vapour concentration. Statistical comparisons of the numerical results over experimental database will be made at the following axial locations: 25, 50, 75, 100 and 150 mm from the exit of the injector assembly unless otherwise stated.

13

3.2. Computational domain

The computational domain, which is represented in Fig. 2, consists of a main inlet for the non-swirling atomising air, a nozzle assembly into which the liquid fuel is delivered, a co-flow inlet, a combustion chamber and an outlet plane. The domain extends 30D and 100D in the radial and axial directions respectively and is discretised using a fully-structured, multi-block mesh with a total number of 1.4 million cells and 162 blocks. The grid resolution comprising 10 computational cells across the main inlet is determined in order for the fluctuating motion of the incoming turbulent flow to be adequately generated. As presented in Fig. 3, a local refinement is made in areas where methanol droplets undergo fragmentation, mixing of fuel vapour with air occurs and jet expansion takes place. The smallest mesh spacing in these regions is around 0.1 mm with an aspect ratio close to unity. The mesh stretching factor is maintained below 10% throughout the entire domain and the largest cell, located in proximity to the exit plane, has a size of approximately 6 mm.
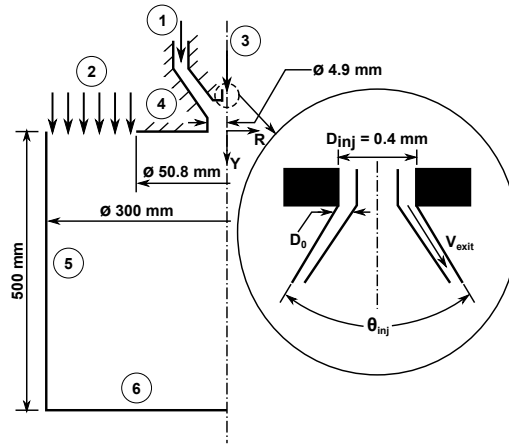
Figure 2: A schematic diagram of the computational domain with boundary conditions highlighted and a sketch of the formation of the liquid film at the final orifice of the simplex injector (not to scale). The boundary conditions applied in the spray computations are as follows: (1) = atomising air inlet, (2) = co-flow inlet, (3) = liquid injection, (4) = no-slip walls, (5) = free slip conditions and (6) = zero-gradient outlet.

3.3. Inlet/boundary conditions

A statistical method, originally developed by Klein *et al.* [78], based on the use of digital filters is adopted in order to represent the structure of a spatially and temporally inhomogeneous turbulent flow through the atomising air inlet (refer to (1) in Fig. 2). The axial velocity component of the air through the co-flow inlet is taken from the measured profiles (≈ 1.0 m/s) at the axial location of 0 mm, *ie* the reference plane collocated with the exit of the nozzle assembly. No-slip wall conditions imposed on the surface of the injector assembly are assumed to be adiabatic as no significant heat loss is expected because of the spray flame being appreciably lifted. Free slip conditions are applied along the outer plane of the computational domain located at 150 mm away from the centreline of the domain. In addition, a zero-gradient outflow boundary condition is applied at the exit plane of the domain. The initial gas temperature and pressure are set to 295.15 K and 1 atm throughout the computational domain while the initial composition of the gas-phase is that of air.

The boundary conditions for the liquid injection are described in the following. The liquid sheet formation suggested in the LISA model [10] is adopted in the present work in order to estimate the initial film thickness and its
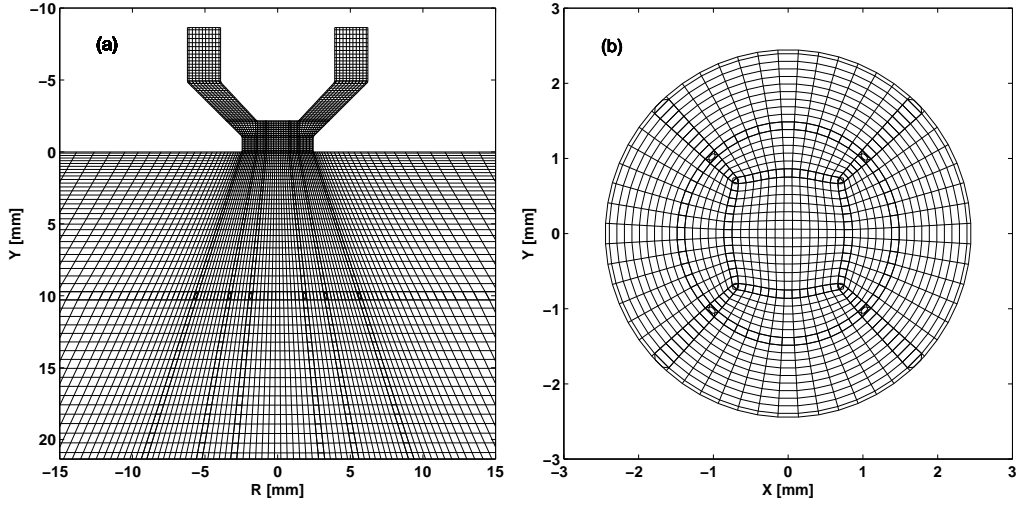
Figure 3: 2-D images of representing grid resolution (a) in the vicinity of the injector assembly and (b) across the jet exit.

total velocity at the exit of the fuel injector. Each droplet being fed into the computational domain is then assigned an initial diameter (D_0) of around 81 μm and a total velocity (V_{exit}) of 22.8 m/s; no droplet size distribution laws such as a Rosin-Rammler distribution are therefore required. Note that the length of the primary breakup which can also be defined by the LISA model is not considered in the present work because the breakup length was found to be around 23 mm, meaning that the dispersion of the smallest drops towards the centreline at the first measurement location (*ie* 25 mm from the nozzle exit) could not be captured. In an analogous manner to other works [11, 13], the stochastic breakup model is applied as a sole closure to represent droplet distributions at axial locations where the breakup process is complete. Conserving the measured mass flow rate of liquid, individual droplets representing the formation of the liquid sheet are injected randomly at 1000 circumferential locations. This injection plane is situated at an axial position corresponding to the actual location of the final injector orifice (Fig. 2). The axial velocity component is assumed to be constant whereas the tangential velocity responsible for the swirling motion inside simplex nozzles is set to vary depending on spray (or injection) angles (θ_{inj}) at which each droplet is injected. The measurements of Marchione *et al.* [79] suggest that the nominal spray angle is not necessarily equal to the measured spray angle and unsteadiness caused by turbulence inside the swirl chamber may be the main reason for the oscillating behaviour of the spray angle. The histogram of the spray angles measured therein reveals the highest probability around the average value of the cone angle; the spray angles are found to vary between 65° and 114° using a simplex nozzle with its nominal spray angle of 80°. The probability then reduces towards the lowest and largest values of the spray angle. There exist no empirical findings to estimate the range of the oscillating spray angles in relation to the geometrical features of pressure-swirl nozzles. In the current work, the standard normal distribution, *ie* $N(0, 1)$, is therefore used to mimic the most likely event around the estimated injection angle of 64° as well as the gradual decrease in *pdf* towards the minimum and maximum injection angles. Figure 4 presents variations of the injection angles collected over 10,000 drops along with the number of counts against the range of the injection angles used ($40° \leq \theta_{inj} \leq 90°$).

3.4. Numerical implementation

All the computational results, which will be presented and discussed in Section. 4, are obtained with the in-house CFD code (BOFFIN-LES). The code is based on a block-structured, parallel, pressure-based flow solver with a low-
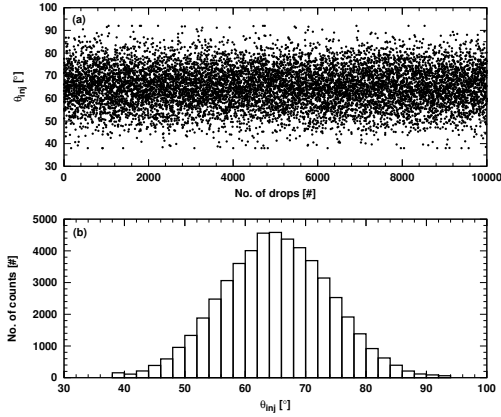
15

Figure 4: (a) variations of injection angle and (b) number of counts versus injection angle.

Mach number, variable density approximation. A Crank-Nicholson method is adopted for time integration while the convective terms in the momentum equation are approximated by a central energy-conserving discretisation scheme. All other spatial derivatives with the exception of the convective terms in the scalar equations are discretised with standard second-order central differences. A Total Variation Diminishing (TVD) scheme is used for the scalars in order to avoid unphysical overshoots and second law violations. The Eulerian stochastic field equations are discretised using the Euler-Maruyama approximation [80], which represents an extension of the standard Euler method for ordinary differential equations to stochastic differential equations. A fractional step method in conjunction with a Newton method are adopted to integrate the stiff chemical rate equations appearing in the stochastic field equations. The performance of this integration constitutes a large fraction of the computational load and to avoid performance loss, the integration work is parallelised further using MPI message passing routines. The stochastic spray equations are solved using a semi-implicit approximation of the form similar to the Euler-Maruyama method. Chemical reaction of methanol-air is described using the reduced, but comprehensive kinetics mechanism of [81] comprising 18 chemical species and 84 reversible elementary steps. This reaction mechanism includes important intermediate species such as CH_2O and CH_3. During the oxidation of oxygenated hydrocarbon species, for example, CH_2O plays a major role as almost all of the carbon atoms in methanol are oxidised through a path including CH_2O [82]. The unknown interaction of sub-grid scale turbulence and chemistry is described by the transported *sgs-pdf* approach with the use of 8 stochastic fields. This number of stochastic field samplings has previously been applied to the investigation of turbulent spray flames [45, 83] and found capable of providing results with a good degree of accuracy.

4. Results and discussion

In this section, a comparison of model predictions with measurements is made and discussed in detail in order to confirm the validity of the Eulerian stochastic field method in conjunction with the stochastic breakup formulation. All the numerical simulations are conducted with a time step of around 0.40 μs, ensuring a maximum CFL number of below 0.30. In order to assess the choice of the numerical setup including the quality of the numerical grid and the inlet/boundary conditions applied to the computational domain, the statistical results obtained from the isothermal case in absence of droplets are first compared in terms the time-averaged mean and fluctuating velocity components of the gas-phase. The computational results obtained using the stochastic breakup model are then presented and

compared in many aspects of the non-reacting spray; its predictive capabilities are, as a consequence, investigated. A qualitative description regarding the structure of the reacting spray that undergoes fragmentation and leads to the formation of the spray flame is given. In the last part, the influence of the flame on the global behaviour of the spray is studied.

4.1. Isothermal case without droplets

A flow-through time of 0.008 seconds corresponding to 20,000 computational time steps is defined based on the bulk velocity at the nozzle exit and the length of the flow domain, *ie* 62.5 m/s and 0.5 m, respectively. The isothermal simulation was initially run for 10 flow-through times in order to flush initial disturbances caused by the initial conditions out of the domain. All the statistical results for the isothermal case without droplets were accumulated over a further 30 flow-through times in order to achieve an adequate level of convergence.

4.1.1. Validation of the numerical setup

Radial profiles of the simulated mean and fluctuating axial gas velocities are compared with measurements in Figs. 5 and 6, respectively. The spreading rate of the air jet, the peak value of the mean axial velocity component along the centreline and the level of turbulence are reproduced at all the measurement locations with a high degree of accuracy. The isothermal case without the presence of droplets displays a typical behaviour of a free jet with a maximum value of u'_Y occurring at a radial distance close to that associated with a peak in the radial gradient of the axial velocity, $d\bar{U}_Y/dR$. This region is known as the shear layer which becomes less pronounced along the axial distance as the air jet decays due to the entrainment of air from the surrounding co-flow.
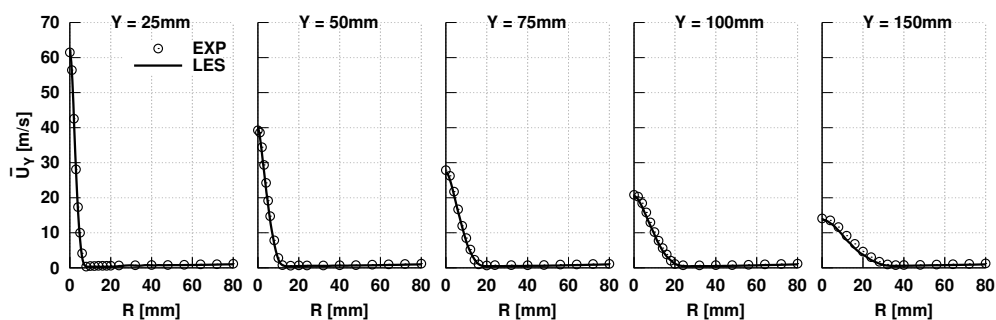
Figure 5: Radial profiles of the mean axial velocities of the gas-phase.

Figures 7 and 8 show a comparison of the time-averaged mean and *rms* quantities of the radial velocity component. Radial profiles of u'_R exhibit trends almost identical to those observed for u'_Y in terms of both the appearance and magnitude. Overall, the predicted statistical quantities are again in excellent agreement with the experimental results apart from a slight under-prediction along the last two measurement locations, *ie* Y = 100 mm to Y = 150 mm. The difference might be attributed to the grid resolution applied in this region being coarser than that applied upstream. However, no effort is made to improve the quality of the grid along the second part of the computational domain as it is likely to lead to a considerable increase in the computational cost. In addition, the ratio of the axial to radial velocity component is so large that no apparent changes in the general pattern of the flow field are expected upon the improvement in the size of the mesh.
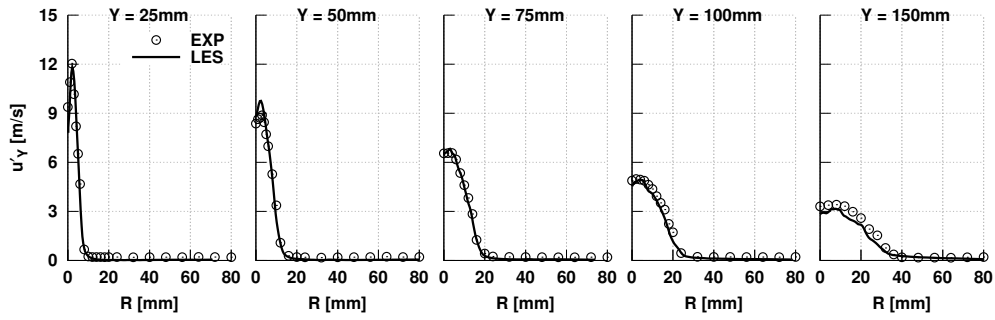
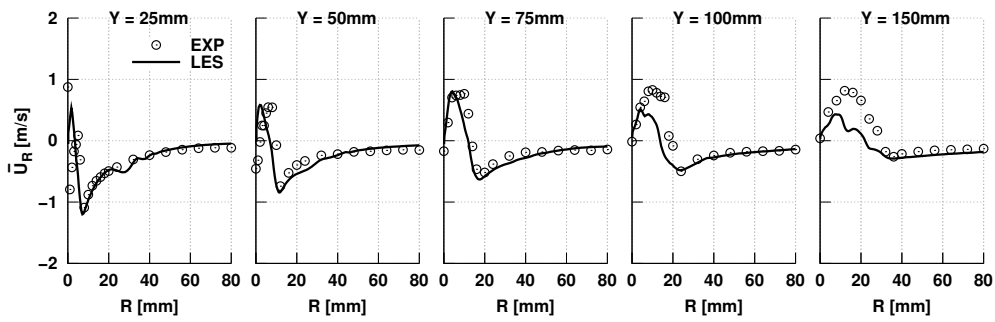Figure 6: Radial profiles of the fluctuating axial velocities of the gas-phase.

Figure 7: Radial profiles of the mean radial velocities of the gas-phase.
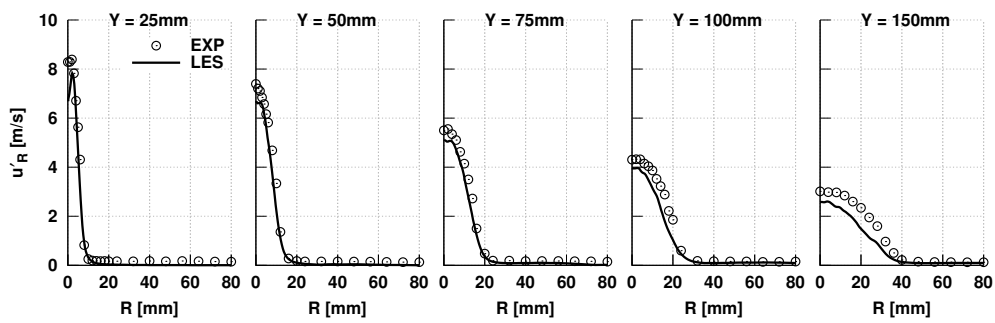

Figure 8: Radial profiles of the fluctuating radial velocities of the gas-phase.

18

The application of the synthetic turbulence generator at the atomising air inlet together with the quality of the computational domain are demonstrated by the excellent agreement achieved between the simulated results and the measurements of the time-averaged gas velocity statistics.

4.2. Non-reacting spray case

The applicability of the stochastic formulation for droplet breakup is tested and validated here against measurements under non-reacting conditions. The non-reacting spray test case was initialised with the flow field taken from the isothermal solution corresponding to 0.027 seconds (or 3 flow-through times) in order to avoid the impact of initial disturbances on the formation of the non-reacting spray. The accumulation of statistics was initiated after another 20 flow-through times were performed in order to ensure that the non-reacting spray reaches a fully-developed state well beyond the last measurement location. All the numerical results which are subject to comparison with the measured profiles were then achieved after the non-reacting spray case was further simulated for 8 flow-through times.

4.2.1. General structure of the non-reacting spray

In order to deliver a general impression on the structure of the non-reacting spray, a contour plot of the instantaneous flow field together with a corresponding snapshot of droplet motions is shown in Fig. 9; a detailed representation of droplet fragmentation occurring in proximity to the nozzle exit is also presented. Initially, droplets having a fixed diameter of around 81 μm equivalent to the calculated liquid sheet thickness are introduced at a range of spray angles varying between 40° and 90°. The droplets being injected into the computational domain undergo breakup and then produce daughter droplets with a wide spectrum of sizes determined by Eq. (30). Depending on the size of a newly formed drop, further disintegration into even smaller drops occurs as a cascading process. Generally speaking, small droplets possessing relatively large velocity fluctuations tend to be quickly convected in towards the centreline due to the entrainment of the co-flow into the air jet imposing an inwardly radial force onto the spray. These small drops with a short relaxation time are highly responsive to the dynamics of the gaseous flow and thus accelerate quickly to the velocity of the gas. Those with larger diameters (*ie* larger inertia), on the other hand, are more likely to follow their initial trajectory for a greater distance. As a result, relatively slow, large drops confined along the edge of the spray (or spray boundary) are observed to surround a central core of small droplets with a higher loading. Many of the large drops are found at radial locations far from the mixing layer of the air jet.

4.2.2. Statistical comparison: Droplet diameters

A quantitative comparison of model predictions with measurements of droplet mean diameters is first presented and discussed. The measured and simulated droplet mean diameters, *ie* the arithmetic mean diameter (D_{10}) and the Sauter mean diameter (D_{32}), are compared in Figs. 10 and 11, respectively. At all the measurement locations, the predicted mean diameters are found to be in good agreement with those measured experimentally in terms of spreading and magnitude. The predicted and measured profiles both exhibit a typical characteristic of those resulting from the application of a hollow-cone simplex atomiser, *ie* a minimum value along the centreline and a maximum value at a certain radial location. This distinct feature occurs due to a partition of droplets depending on their resistance to momentum transfer from the gaseous flow. The increase of the maximum mean diameters along the furthermost radial positions, observed in both the LES simulation and the experiment, is caused by droplet dispersion; the convection of small droplets with less inertia towards the centreline continues in the streamwise direction and a higher population of large drops thus appears along the spray boundary. At the last measurement location (Y = 150 mm), the gradient at which both D_{10} and D_{32} increase in the radial direction is computed to be steeper in the spray calculation. This
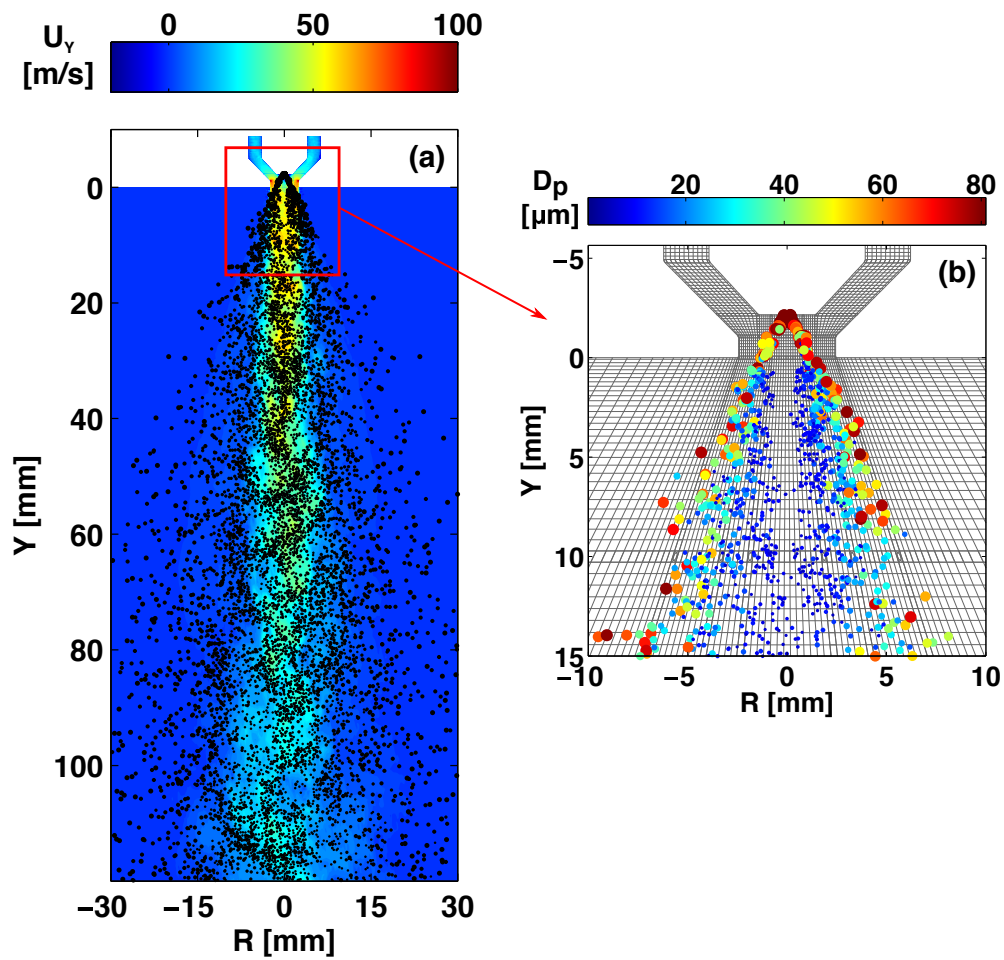
Figure 9: (a) The instantaneous gas-phase velocity field with droplet motions and (b) a detailed view of breakup processes near the atomiser. Note that the appearance of droplets is scaled according to their size.

over-prediction is caused by the radial velocity of the spray being underestimated between the last two measurement locations. The outwards radial spreading of droplets, as a consequence, is less pronounced in the LES computation. More discussion on this will be made in the following subsection.
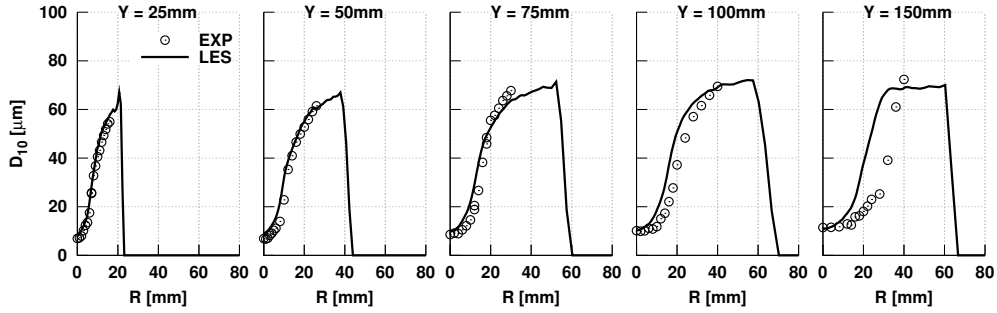
Figure 10: Radial profiles of the arithmetic mean diameter (D_{10}).
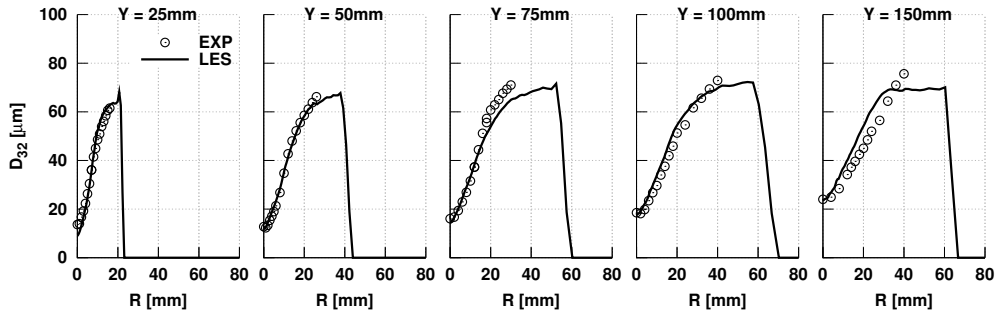
Figure 11: Radial profiles of the Sauter mean diameter (D_{32}).

4.2.3. Statistical comparison: Droplet velocity behaviour

The dynamics of the non-reacting spray are now discussed. The simulated mean and fluctuating axial velocity statistics, which are collected by considering all droplet size classes, are first compared with the experimental results as shown in Figs. 12 and 13, respectively. An excellent reproduction of the time-averaged mean spray velocities is achieved at all the axial locations while the *rms* fluctuations of the axial velocity component of the spray are generally in good agreement with the measured profiles, with the exception of the outer half of the profiles at axial distances beyond Y = 75 mm where the simulated values are too low. The cause of these low values can be explained as follows. A fraction of droplets with small sizes, which were experimentally observed to travel along the spray boundary, are found to be fully convected in towards the centreline in the LES simulation. As a consequence, they do not contribute to the fluctuations in the outer part of the spray, leading to the low simulated values away from the centreline.

The computed mean radial spray velocities, as presented in Fig. 14, agree reasonably well with measurements until the last measurement location by which the simulated radial spray velocities decay effectively to zero. This could be a consequence of the simulated radial velocity component of the gaseous flow which is also found to be lower in comparison to that measured (recall the discussion made in Sec. 4.1.1). The simulated radial component of the spray velocities being too low is also responsible for the dispersion of a smaller number of droplets away from the centreline
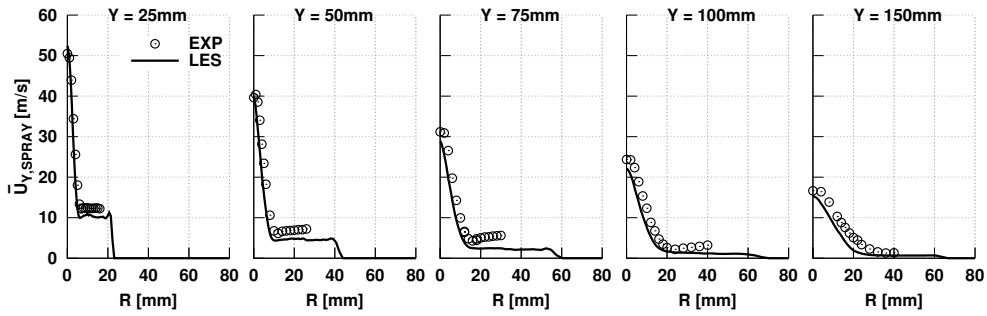
21

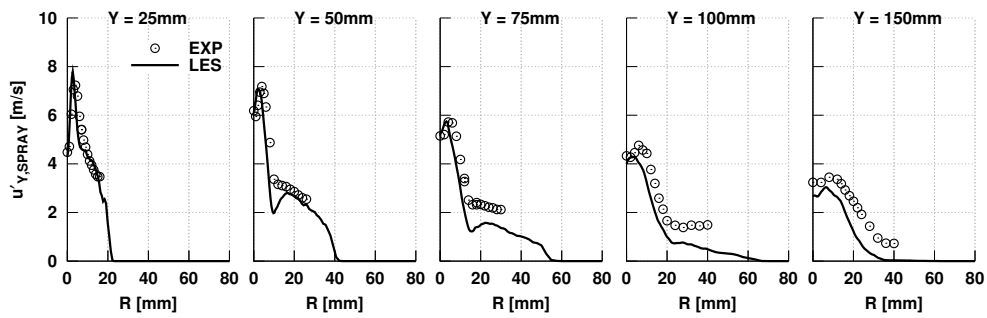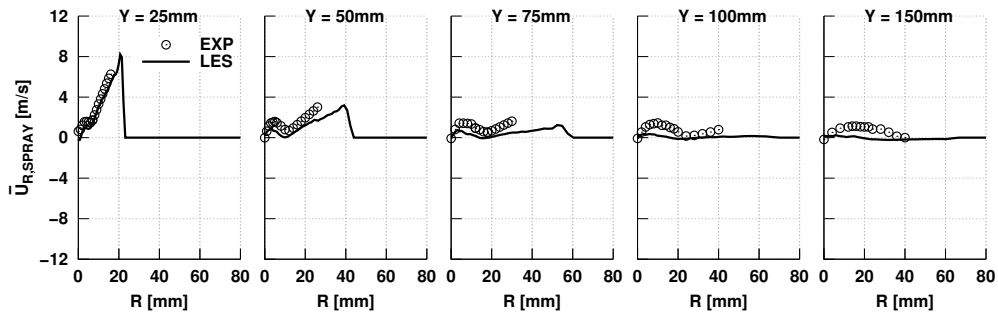Figure 12: Radial profiles of the mean axial velocities for all droplet size classes.

Figure 13: Radial profiles of the fluctuating axial velocities for all droplet size classes.

than that observed experimentally. In other words, the outwardly radial spreading of the spray is less pronounced. As a consequence, the simulated mean droplet diameters are too high whereas the *rms* fluctuations of both the axial and radial spray velocities in the vicinity of the spray boundary are too low. As anticipated, the magnitude of the radial component of the fluctuating spray velocities is found to be less than that measured across the two most downstream measurement locations. Apart from this discrepancy, the simulated results are generally in reasonable agreement with the experimental results.

Figure 14: Radial profiles of the mean radial velocities for all droplet size classes.

22
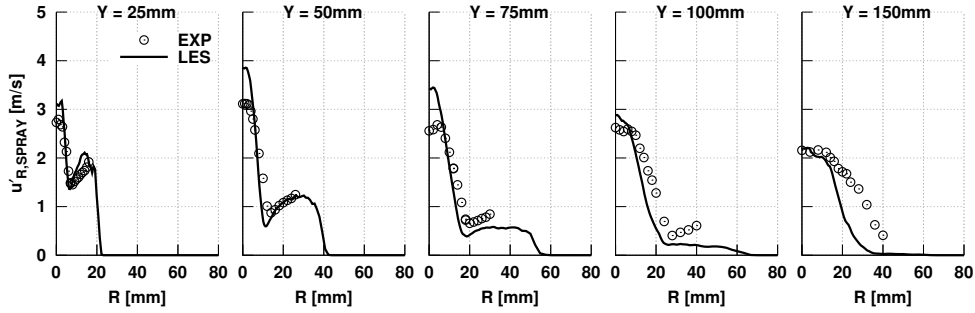
Figure 15: Radial profiles of the fluctuating radial velocities for all droplet size classes.

4.2.4. Statistical comparison: correlation between size and velocity

The axial component of the mean droplet velocities, as a function of three different size classes (D = 11-20 μm, D = 31-40 μm and D = 51-60 μm), is analysed in order to investigate if there exists a mutual relationship between droplet size and velocity. In Fig. 16, the simulated mean droplet velocities conditioned on different droplet sizes are compared with measurements - the gas-phase velocity statistics are also presented for the purpose of comparison. Close to the fuel injector and in the region Y ≤ 50 mm, a strong correlation between droplet size and velocity prevails; larger droplets, which can maintain their initial momentum for a longer period, exhibit a significant slip velocity with respect to the gaseous flow whilst those within the smallest size class are more likely to follow the dynamics of the gas-phase. In general, this size-velocity correlation is well reproduced. Along the edge of the spray, however, the presence of the smallest droplets is not captured in the LES simulation. The following could, in part, provide an explanation for this disagreement. In the experiment, a portion of small droplets 'torn off' the outer edge of the liquid film travel at a location away from the centreline. This phenomenon cannot be reproduced in the spray computation with discrete droplets as all the smallest drops are quickly convected towards the centreline. In the vicinity of the spray centreline, both the measured and simulated axial gas-phase velocities are found to exceed all the conditional droplet velocities, indicating that momentum is mainly transferred from the spray to decelerate the gaseous flow. The deceleration of the gas-phase owing to the presence of the non-reacting spray at the centreline is well captured, as is evidenced by the accurate reproduction of the maximum velocities at axial locations Y < 75 mm. Beyond Y = 75 mm, on the other hand, the strong correlation of droplet size with velocity is no longer apparent because of a relatively long time for droplets to reach this axial distance. A long-exposure of large droplets to the gas-phase results in a relaxation of the relative velocity to effectively zero, implying that momentum transfer is minimal in the downstream part of the spray.

4.2.5. Local droplet dynamics

The detailed comparison of the simulated results with measurements has been presented and discussed in terms of the time-averaged behaviour of the spray thus far. However, it is also important to correctly reproduce the instantaneous structure of the spray. A further assessment of the predictive capabilities of the present breakup model is therefore made by examining a local, time-resolved collection of the droplet dynamics at two radial locations, *ie* R = 0 and 24 mm, at Y = 75 mm. At the centreline, as presented in Fig. 17, the range of droplet sizes collected in the LES simulation is found to fall well within that measured experimentally. The clustering of droplets, associated with either atomisation or the aerodynamics of the flow [84], is both computationally and experimentally established
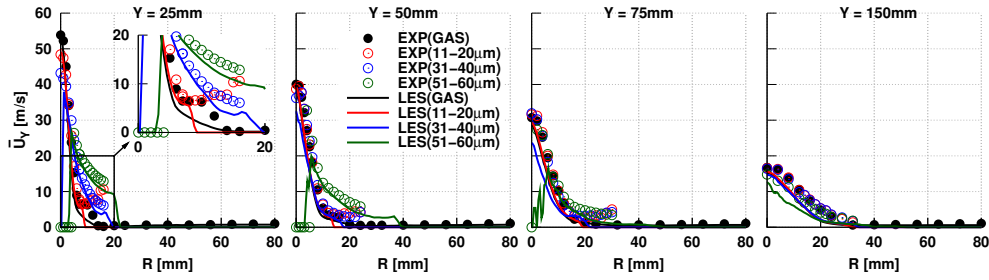
Figure 16: Radial profiles of the mean axial velocities for different droplet size classes and for gas.

(Fig. 17b). The visible evidence of the clustering, possibly in response to the flow pattern of the gaseous flow, can be observed in Fig. 9. The computational investigation of Squires and Eaton [85] also suggests that the clustering might be attributable directly to the aerodynamics of the surrounding flow field. As can be seen in Fig. 18, droplet arrival at the edge of the spray (R = 24 mm) is, to some extent, more consistent than it is at the centreline. However, the local voids where no droplets are present as well as the clustering of droplets are detected, in both the experiment and the spray computation, to repeat in a random fashion throughout the entire period of the time series collection. This kind of droplet arrival is not desirable since local fluctuations of stoichiometry affecting either the stability of the flame or the rate of pollutant formation can arise [84].
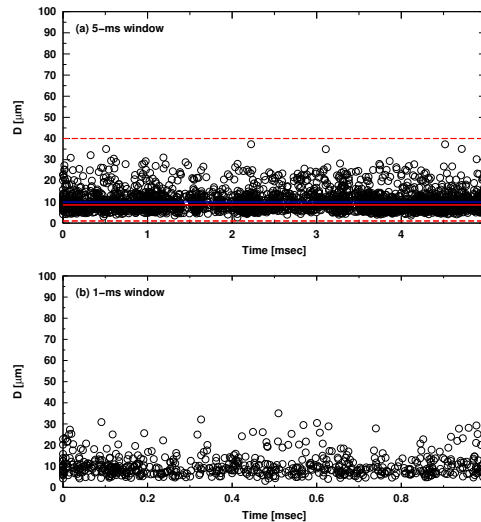

Figure 17: Time series collection of drop sizes at Y = 75 mm and R = 0 mm: (a) 5-ms window and (b) 1-ms window. Red solid and dashed lines indicate the arithmetic mean diameter and the range of drop diameters obtained in the experiment while blue solid line represents the predicted mean diameter over the collected drops.

4.3. Reacting spray case

Having achieved an accurate representation of the general behaviour of the non-reacting spray with the use of the stochastic breakup model, the reacting spray case is now considered. The spray flame calculation was initiated with a non-reacting solution obtained after 0.018 seconds (or 2 flow-through times). In order to establish the stable anchoring
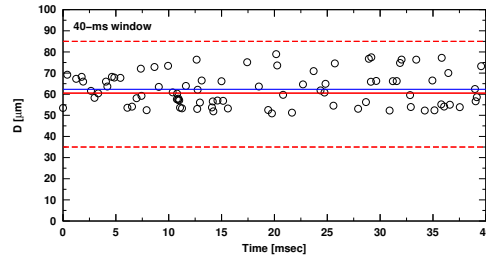
24

Figure 18: Time series collection of drop sizes at Y = 75 mm and R = 24 mm: 40-ms window. Lines indicate the same variables as in Fig. 17.

of a lifted flame, the reacting spray case was further simulated for around 12 flow-through times. The statistical results, which are to be compared against the experimental results, were obtained after another 3 flow-through times to achieve a reasonable level of convergence in the quantities of interest.

4.3.1. General spray flame structure

Prior to presenting a statistical comparison between the numerical and experimental results, the general structure of the methanol/air spray flame is first examined in depth. In the experiment, a type R thermocouple was employed to obtain gas temperature measurements in regions away from the reacting spray. It is unfortunate, however, that the temperature measurements were reported to have large errors in the region close to the high-velocity atomising air jet and droplets [34]; the experimental results are therefore only qualitative. Although no direct comparison of the computed gas temperature field with measurements is made in this work, the simulated results are presented as an aid to the interpretation of the formation of a distinctive flame structure that develops in association with the use of pressure-swirl nozzles.

A contour plot of the instantaneous gas temperature field with a corresponding snapshot of the reacting spray is presented in Fig. 19. The reproduction of the structure of this methanol spray flame using the *pdf* approach is found to be, at least qualitatively, in good agreement with that observed experimentally in terms of the following features. The structure of the reacting spray in regions near the atomising nozzle exit remains almost identical to the behaviour of the non-reacting spray; the formation of a central core with small droplets in proximity to the spray centreline and the surrounding of the core by relatively large droplets travelling along the spray boundary. It can therefore be argued that spray atomisation process in this particular burner is not influenced by the presence of the spray flame because this zone corresponds to a region where the breakup of liquid fuel primarily occurs without an apparent sign of combustion and is complete prior to the onset of burning. Further downstream, starting from an axial location of roughly 50-60 mm, the reacting spray begins to develop a feature distinct from that in the non-reacting spray. A local void of large droplets away from the centreline can be observed, which was believed to coincide with the location of the reaction zone [34]. The central core travels relatively far downstream, but becomes fully evaporated at an axial distance corresponding to a region where the reaction zone has penetrated to the centreline.

4.3.2. Examination of turbulent spray flame structure

The morphology of the reaction zone numerically observed in the spray flame of interest is further investigated and qualitatively compared to other experimental works [86, 87, 88] where lifted turbulent spray flames were studied using pressure-swirl atomisers. Lifted gaseous flames develop a single reaction zone, the structure of which may be explained by triple flame arguments - a detailed description of triple flames can be found in [89]. Idealised triple flames
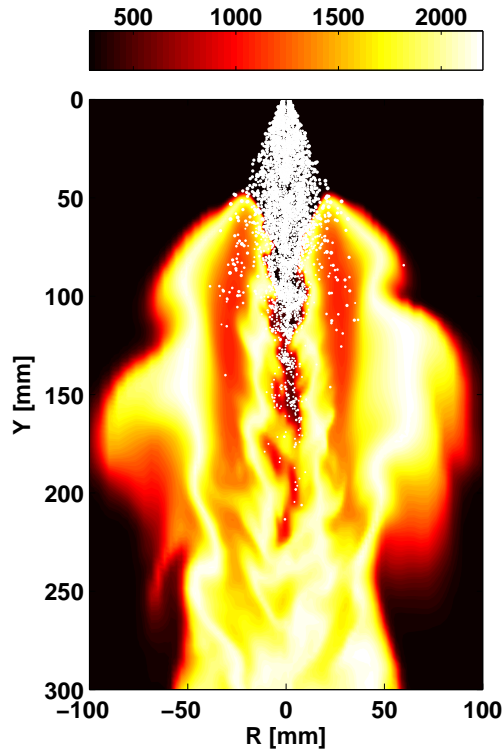
25

Figure 19: A contour plot of the instantaneous gas-phase temperature with the reacting spray.

are composed of fuel-lean and fuel-rich premixed flames together with the appearance of a trailing diffusion flame at the intersection of the two premixed wings. In theory, the stabilisation of this diffusion flame extending downstream is achieved by the two premixed branches which permit flame propagation against the incoming unburnt mixture. This theoretical flame structure has been confirmed experimentally in [87]. The fuel-lean premixed flame branch witnessed in CH planar laser-induced fluorescence (PLIF) images plays an important role in the flame stabilisation as it is found to protrude radially outwards at the flame base (or the leading edge). On the other hand, the fuel-rich premixed branch that is not apparent in CH-PLIF images is believed to have merged into the trailing diffusion flame due to the relatively high-speed fuel jet. It is therefore said that the leading-edge combustion in lifted gaseous flames exhibits a distorted triple flame [87]. In contrast, the turbulent spray flame under consideration reveals a double (or dual) reaction zone structure as a result of the polydisperse spray emerging from the simplex atomiser.

Two contour plots of the instantaneous mass fraction of OH with particle motions in regions close to the leading-edge of the flame are presented in Fig. 20. The leading-edge combustion observed through the application of the Eulerian stochastic field method clearly shows features different from lifted turbulent gaseous flames. The development of the double reaction zone is apparent and is associated with two conical-shape flame fronts diverging radially inwards or outwards on each side of the spray centreline. Each of the two flame fronts originates from the same flame base, the height of which can be referred to as a stabilisation point. The inner flame front corresponds to a reaction zone which develops along the turbulent shear layer in proximity to the spray centreline while the outer flame front is situated in regions of the low-speed co-flow. The simulated OH contour plots are in good agreement with the experimental observation that the outer reaction zone, which is well isolated from the structure of large-scale turbulence,

26

tends to be stable and to show a less wrinkled OH contour [88]. Relatively large droplets with high momentum are more likely to penetrate the flame front along the inner reaction zone and then evaporate rapidly between the dual structure; this region provides a fuel vapour source for the stable outer diffusion flame [90]. The simulated OH mass fraction which appears as a thin band along the stoichiometric mixture is an additional evidence that the outer reaction zone may exhibit a typical characteristic of diffusion flames [91].

The flame morphology of the inner reaction zone in the vicinity of the leading-edge is found to possess clear differences in comparison to that of the stable outer flame front; the inner zone burning in a diffusion-like mode [86] is highly wrinkled and corrugated because of the interaction of large-scale turbulent motions with the flame front. At downstream locations, the flame undergoes transition to a partially premixed combustion mode owing to turbulent mixing along the shear layer. The broadening of the simulated OH contour confirms this transition from a diffusion like to a partially premixed flame. In premixed or partially premixed combustion, the widening of the OH signal occurs as OH radicals are present within the hot combustion products [90]. It may thus be inappropriate to employ OH-PLIF imaging techniques when determining the location of the reaction zone under these combustion regimes. The thickness of the inner reaction zone is observed to be noticeably thinner than that of the outer diffusion flame. The relatively thin OH contour might be attributed to the fact that this inner combustion occurs in regions of relatively high strain rates while the outer reaction zone burns in the low-velocity co-flow. There are two essential mechanisms involved in flame stabilisation in this configuration; (i) the presence of small droplets to produce a mixable fuel vapour and (ii) rapid mixing of the fuel vapour with air through large-scale turbulence. The smallest droplets with high evaporation rates are found to disperse in regions between the spray centreline and the turbulent shear layer and to produce the fuel vapour, which is then consumed to maintain the inner flame front. The spray flame is observed to stabilise at an axial location of roughly 50 mm away from the nozzle exit, a value to be compared with the measured lift-off height of 50 to 60 mm [34].

In order to better understand the structure of the spray flame, scatter plots of mixture fraction and temperature together with their *pdf* at three different flame locations are examined in Fig. 21. The location of LES probes, as highlighted in Fig. 20, is chosen such that the initial mode of the inner reaction zone and its downstream transition into the partially premixed mode can be analysed. In addition, the structure of the outer flame front is investigated along its entire length. Apparently, the inner flame in the vicinity of the stabilisation point (P1) appears to possess a complex flame structure with the coexistence of both premixed and diffusion combustion modes. Although the *pdf* of the mixture fraction around the stoichiometric mixture fraction (Z_{st}) of 0.136 is slightly higher, the occurrence of a lean premixed flame is evident. The presence of the two flame modes along the initial inner flame is also captured numerically in a lifted spray flame [92]. At the downstream location (P2), the influence of turbulent mixing on the structure of the inner reaction zone can be clearly seen as the dispersion of the mixture fraction in the temperature space becomes wider. The higher *pdf* towards the mixture fraction well below its stoichiometric value supports that the inner flame at this axial location burns mostly in fuel lean conditions. The outer reaction zone exhibits a similar pattern to that of the initial inner flame in terms of the *pdf* of the temperature, but shows a much higher maximum *pdf* around the stoichiometric mixture; this indicates that the outer flame reacts in a pure diffusion mode.

4.3.3. Influence of spray flame on droplet distributions

In Figs. 22 and 23, the statistical results in terms of the mean droplet diameters (D_{10} and D_{32}) are compared to measurements (for the purpose of comparison, the results from the non-reacting spray case are also included). The simulated and measured droplet distributions at the first three measurement locations, *ie* up to Y = 50 mm, remain almost identical for the reacting and non-reacting cases as no reaction takes place in this region of the spray. At Y =
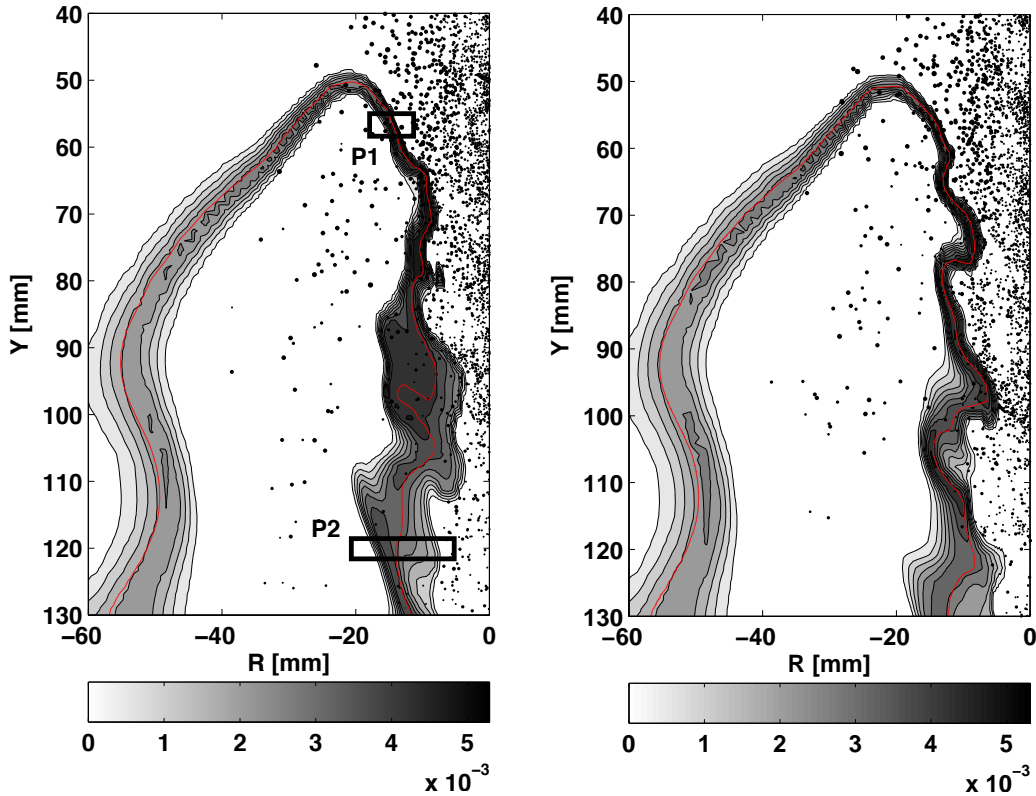
Figure 20: Instantaneous mass fraction of OH together with the corresponding droplet motions and the stoichiometric mixture fraction highlighted in red solid lines. The location of two LES probes for flame structure analysis is also highlighted.

75 mm, a considerable reduction in the mean diameters begins to become evident at radial locations away from the spray centreline. This reduction is indicative of the initiation of combustion upstream this axial location, consistent with the OH images. There exists a significant difference between the two cases at Y = 100 mm; the radial location at which these differences become apparent moves towards the spray centreline and a smaller number of droplets travel away from the centreline due to their relatively long residence time within the hot combustion products. At Y = 150 mm, only a few droplets are present in the region close to the centreline and a further reduction in the mean diameters is well reproduced.

4.3.4. Influence of spray flame on droplet velocity

The effects of the spray flame on the behaviour of droplet dynamics are now discussed. Again, radial profiles of the mean axial and radial velocities for all droplet size classes, as presented in Figs. 24 and 25, display identical results between the reacting and non-reacting cases along the measurement locations up to Y = 50 mm. The influence of the reaction on both the mean axial and radial spray velocities becomes apparent away from the spray centreline at Y = 75 mm; the reacting spray velocities are observed to be higher than those of the non-reacting spray. The increase in the magnitude of the velocity is attributable to the expansion of the gas-phase associated with chemical reaction. The acceleration of the reacting spray is reasonably well represented at the downstream measurement locations.
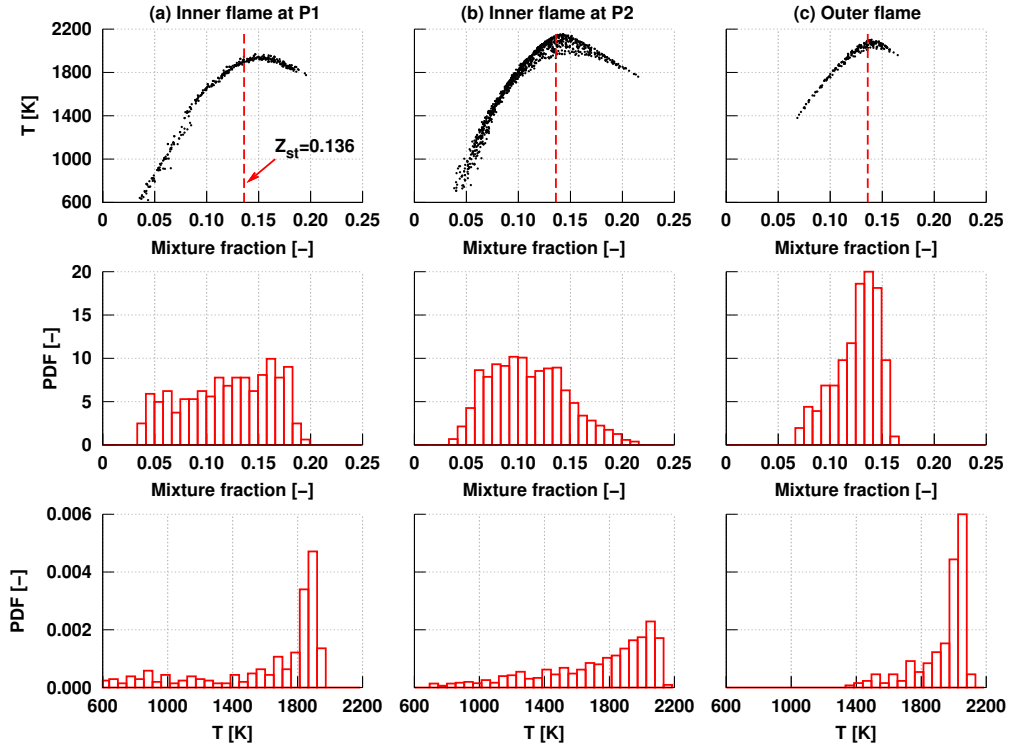
28

Figure 21: Comparison of scatter plots of mixture fraction and gas-phase temperature (top row), *pdf* of mixture fraction (middle row) and *pdf* of temperature (bottom row) at three different flame locations. Note that data collection is performed only when reaction takes place across the LES probes.
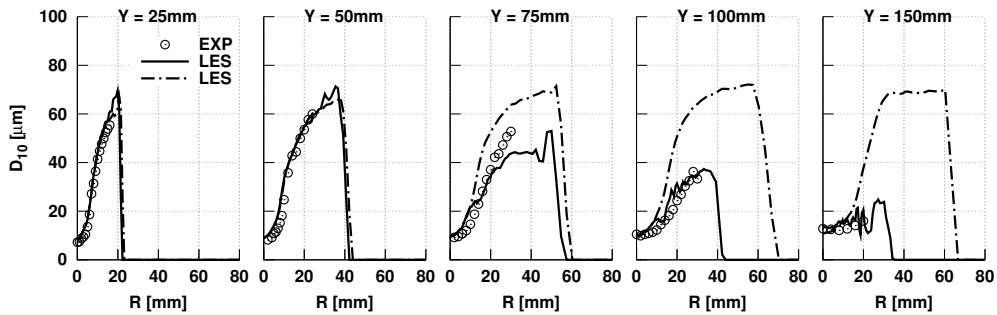

Figure 22: Radial profiles of the arithmetic mean diameter (D_{10}); measurements (○), non-reacting LES (– · –) and reacting LES (——).
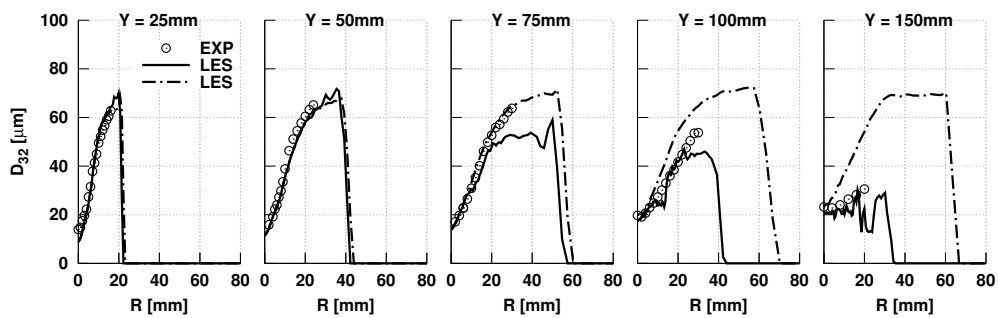
Figure 23: Radial profiles of the Sauter mean diameter (D_{32}); measurements (○), non-reacting LES (– · –) and reacting LES (——).
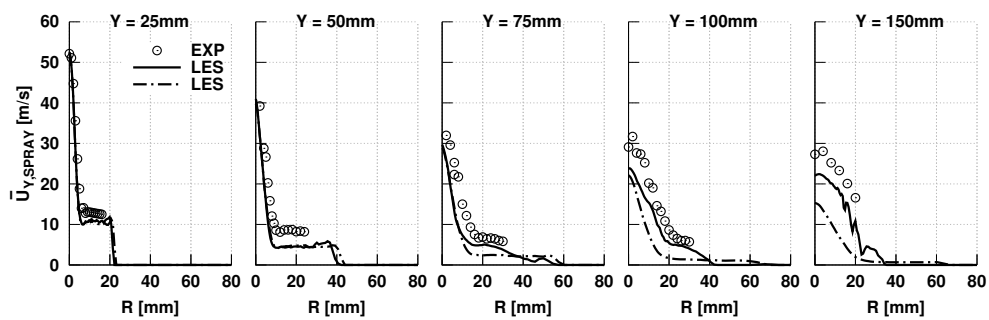

Figure 24: Radial profiles of the mean axial velocities for all droplet size classes; measurements (○), non-reacting LES (– · –) and reacting LES (——).

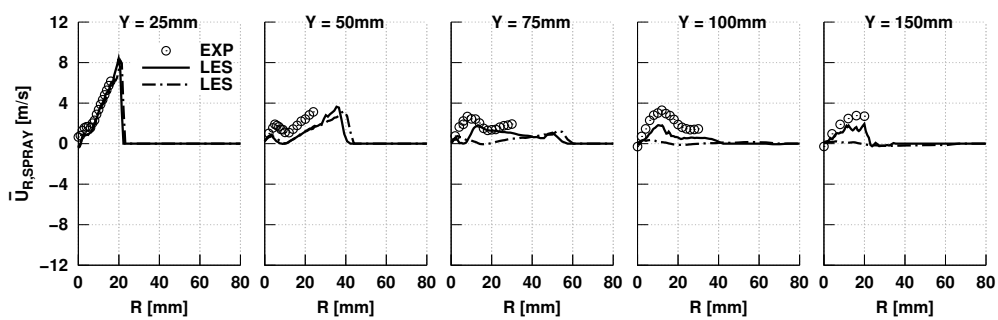Figure 25: Radial profiles of the mean radial velocities for all droplet size classes; measurements (○), non-reacting LES (– · –) and reacting LES (——).

5. Conclusions

In the present investigation, a stochastic breakup model is formulated and applied, in conjunction with the sub-grid scale *pdf* formulation, to LES simulations of a turbulent methanol/air spray flame. A fully-coupled, stochastic Lagrangian particle methodology is employed to represent the probabilistic behaviour of the spray undergoing dispersion, evaporation and atomisation. Gas-phase turbulence-chemistry interactions are described by *sgs-pdf* transport equation/stochastic fields method together with a reduced, but comprehensive reaction mechanism for the oxidation of methanol involving 18 reactive species and 84 elementary reaction steps. The results obtained from LES computations are compared with existing detailed measurements of the gas-phase with and without droplets and spray characteristics under non-reacting and reacting conditions. LES is shown to provide an accurate reproduction of the mean and fluctuating turbulent flow field in the isothermal case without droplets. The statistical results for the non-reacting spray case are found to be, both locally and globally, in excellent agreement with measurements in terms of the dispersion of the spray, the mean droplet diameters, the mean spray velocities and the correlation between drop size and velocity. The stochastic breakup model, with improvements in the breakup frequency, the daughter droplet size *pdf* and the determination of the expected droplet life time through the discrete Poisson process, has therefore demonstrated its predictive capabilities in the modelling of spray atomisation arising from low pressure, swirl nozzles. The revised breakup model may be employed in place of the trial and error procedure that is often used to match the measured downstream profiles of droplet velocity and size distributions and in situations where no such measurements exist. Based on the examination of OH contour plots together with scatter plots of temperature and mixture fraction, the turbulent spray flame of interest is observed to exhibit the following features:

- In contrast to turbulent lifted gaseous flames with the appearance of a single reaction zone, the leading-edge of the spray flame develops a double reaction zone as a result of the polydisperse spray emerging from the simplex atomiser.

- The inner flame front initially burning in diffusion-like mode and then under partially premixed condition at downstream locations is observed to be highly wrinkled due to its interaction with large-scale turbulence while the outer combustion zone occurring in regions of the low-speed coflow tends to be stable and relatively smooth.

- A complex flame pattern along the inner flame is revealed with the occurrence of both diffusion and lean premixed flame modes whereas the outer reaction zone burns as a pure diffusion flame.

- The presence of small droplets that follow the turbulent shear layer is responsible for flame stabilisation along the inner flame structure as they readily evaporate and create a fuel vapour source for enhanced mixing (due to large-scale turbulent structures) and combustion. On the other hand, large droplets, penetrating the inner flame front, provide the fuel vapour between the double flame structure which is then consumed to maintain the stable outer diffusion flame.

- The location of the leading-edge (also called lift-off height) is found to agree well with the measured value.

In addition, the influence of the flame on the behaviour of the spray is reasonably well captured in terms of a reduction in the mean droplet diameters and the increased spray velocities in response to the expansion of the gas-phase during the reaction. Future work may include the application of the present approach to investigate the effects of the swirling atomising air on the structure of a spray flame and the LES methodology presented in this paper can be considered a promising candidate for modelling of other spray flames using pressure-swirl atomisers.

Acknowledgement

References

[1] A. Lefebvre, Atomisation and Sprays, CRC Press, 1988

[2] L. P. Bayvel, Liquid Atomisation, CRC Press, 1993

[3] M. Pilch, C. A. Erdman, Use of breakup time data and velocity history data to predict the maximum size of stable fragments for acceleration-induced breakup of a liquid drop, Int. J. Multiphase Flow 13 (6) (1987) 741–757.

[4] L. Hsiang, G. M. Faeth, Near-limit drop deformation and secondary breakup, Int. J. Multiphase Flow 18 (5) (1992) 635–652.

[5] N. Dombrowski, R. P. Fraser, A photographic investigation into the disintegration of liquid sheets, Phil. Trans. Roy. Soc. London 247A (1954) 101–130.

[6] R. P. Fraser, P. Eisenklam, N. Dombrowski, D. Hasson, Drop formation from rapidly moving liquid sheets, AIChE J. 8 (5) (1962) 672–680.

[7] H. B. Squire, Investigation of the instability of a moving liquid film, Br. J. Appl. Phys. 4 (6) (1953) 167–169.

[8] N. Dombrowski, W. R. Johns, The aerodynamic instability and disintegration of viscous liquid sheets, Chem. Eng. Sci. 18 (3) (1963) 203–214.

[9] D. P. Schmidt, I. Nouar, P. K. Senecal, J. K. Rutland, R. D. Reitz, Pressure-Swirl Atomisation in the Near Field, SAE Technical Paper (1999)

[10] P. K. Senecal, D. P. Schmidt, I. Nouar, C. J. Rutland, R. D. Reitz, M. L. Corradini, Modelling high-speed viscous liquid sheet atomisation, Int. J. Multiphase Flow 25 (6) (1999) 1073–1097.

[11] P. J. O'Rourke, A. A. Amsden, The TAB method for numerical calculation of spray droplet breakup, Tech. rep., SAE Technical Paper (1987).

[12] R. D. Reitz, Modelling atomisation processes in high-pressure vaporizing sprays, Atomisation Spray Technology 3 (1987) 309–337.

[13] S. V. Apte, M. Gorokhovski, P. Moin, LES of atomizing spray with stochastic modelling of secondary breakup, Int. J. Multiphase Flow 29 (9) (2003) 1503–1522.

[14] W. P. Jones, C. Lettieri, Large eddy simulation of spray atomisation with stochastic modelling of breakup, Phys. Fluids 22 (11) (2010) 115106.

[15] S. W. Park, S. Kim, C. S. Lee, Breakup and atomisation characteristics of mono-dispersed diesel droplets in a cross-flow air stream, Int. J. Multiphase Flow 32 (7) (2006) 807–822.

[16] H. Hiroyasu, T. Kadota, Fuel droplet size distribution in diesel combustion chamber, Bulletin of JSME 19 (135) (1976) 1064–1072.

[17] P. Moin, S. V. Apte, Large-eddy simulation of realistic gas turbine combustors, AIAA Journal 44 (4) (2006) 698–708.

[18] A. Irannejad, A. Banaeizadeh, F. Jaberi, Large eddy simulation of turbulent spray combustion, Combust. Flame 162 (2) (2015) 431–450.

[19] J. Smagorinsky, General circulation experiments with the primitive equations: I. The basic experiment, Monthly Weather Review 91 (3) (1963) 99–164.

[20] D. K. Lilly, The representation of small scale turbulence in numerical simulation experiments, in: IBM Scientific Computing Symposium on Environmental Sciences, 1967, 195–210.

[21] H. Pitsch, Large-eddy simulation of turbulent combustion, Annu. Rev. Fluid Mech. 38 (2006) 453–482.

[22] F. Gao, E. E. O'Brien, A large-eddy simulation scheme for turbulent reacting flows, Phys. Fluids A: Fluid Dynamics 5 (6) (1993) 1282.

[23] S. B. Pope, PDF methods for turbulent reactive flows, Prog. Energy Combust. Sci. 11 (2) (1985) 119–192.

[24] L. Valiño, A field Monte Carlo formulation for calculating the probability density function of a single scalar in a turbulent flow, Flow Turbul. Combust. 60 (2) (1998) 157–172.

[25] V. Sabel'nikov, O. Soulard, Rapidly decorrelating velocity-field model as a tool for solving one-point Fokker-Planck equations for probability density functions of turbulent reactive scalars, Phys. Rev. E 72 (1) (2005) 016301.

[26] R. Mustata, L. Valiño, C. Jiménez, W. P. Jones, S. Bondi, A probability density function Eulerian Monte Carlo field method for large eddy simulations: application to a turbulent piloted methane/air diffusion flame (Sandia D), Combust. Flame 145 (1) (2006) 88–104.

[27] W. P. Jones, S. Navarro-Martinez, Large eddy simulation of autoignition with a subgrid probability density function method, Combust. Flame 150 (3) (2007) 170–187.

[28] W. P. Jones, V. N. Prasad, Large Eddy Simulation of the Sandia Flame Series (D-F) using the Eulerian stochastic field method, Combust. Flame 157 (9) (2010) 1621–1636.

[29] T. Brauner, W. P. Jones, A. J. Marquis, LES of a Stratified Swirl Burner using a sub-grid Pdf Approach, Flow Turbul. Combust. 96 (2016) 965–985.

[30] G. Bulat, W. P. Jones, A. J. Marquis, Large Eddy Simulation of an industrial gas-turbine combustion chamber using the sub-grid PDF method, Proc. Combust. Inst. 34 (2) (2013) 3155–3164.

[31] W. P. Jones, S. Lyra, S. Navarro-Martinez, Large Eddy Simulation of a swirl stabilized spray flame, Proc. Combust. Inst. 33 (2) (2011) 2153–2160.

[32] W. P. Jones, A. Tyliszczak, Large eddy simulation of spark ignition in a gas turbine combustor, Flow Turbul. Combust. 85 (3-4) (2010) 711–734.

[33] V. N. Prasad, A. R. Masri, S. Navarro-Martinez, K. H. Luo, Investigation of auto-ignition in turbulent methanol spray flames using Large Eddy Simulation, Combust. Flame 160 (12) (2013) 2941–2954.

[34] V. McDonell, M. Adachi, G. S. Samuelsen, Structure of reacting and nonreacting, non-swirling, air-assisted sprays, Part I: Gas-phase properties, Atomisation Sprays 3 (4) (1993) 389–410.

[35] V. McDonell, M. Adachi, G. S. Samuelsen, Structure of reacting and nonreacting, non-swirling, air-assisted sprays, Part II: Drop behaviour, Atomisation Sprays 3 (4) (1993) 411–436.

[36] C. Hollmann, E. Gutheil, Modelling of turbulent spray diffusion flames including detailed chemistry, Symp. (Int.) Combust. 26 (1996) 1731–1738.

[37] C. Hollmann, E. Gutheil, Diffusion flames based on a laminar spray flame library, Combust. Sci. Technol. 135 (1-6) (1998) 175–192.

[38] H.-W. Ge, E. Gutheil, Probability density function (pdf) simulation of turbulent spray flows, Atomisation Sprays 16 (5).

[39] H.-W. Ge, E. Gutheil, Simulation of a turbulent spray flame using coupled PDF gas-phase and spray flamelet modelling, Combust. Flame 153 (1) (2008) 173–185.

[40] H.-W. Ge, Y. Hu, E. Gutheil, Joint gas-phase velocity-scalar PDF modelling for turbulent evaporating spray flows, Combust. Sci. Technol. 184 (10-11) (2012) 1664–1679.

[41] A. Favre, Turbulence: Space-time statistical properties and behaviour in supersonic flows, Phys. Fluids (1958-1988) 26 (10) (1983) 2851–2863.

[42] M. Germano, U. Piomelli, P. Moin, W. H. Cabot, A dynamic subgrid-scale eddy viscosity model, Phys. Fluids A: Fluid Dynamics (1989-1993) 3 (7) (1991) 1760–1765.

[43] C. Dopazo, Probability density function approach for a turbulent axisymmetric heated jet. Centerline evolution, Phys. Fluids 18 (4) (1975) 397.

[44] J. Villermaux, J. C. Devillon, Représentation de la coalescence et de la redispersion des domaines de ségrégation dans un fluide par un modèle d'interaction phénoménologique, in: Proceedings of the 2nd International symposium on chemical reaction engineering, Elsevier New York, 1972,. 1–13.

[45] W. P. Jones, A. J. Marquis, D. Noh, LES of a methanol spray flame with a stochastic sub-grid model, Proc. Combust. Inst. 35 (2) (2015) 1685–1691.

[46] C. W. Gardiner, Handbook of Stochastic Methods for Physics, Chemistry, and the Natural Sciences, Springer, 2004.

[47] M. Bini, W. P. Jones, Large-eddy simulation of particle-laden turbulent flows, J. Fluid Mech. 614 (2008) 207–252.

[48] M. R. Maxey, J. J. Riley, Equation of motion for a small rigid sphere in a nonuniform flow, Phys. Fluids (1958-1988) 26 (4) (1983) 883–889.

[49] M. Bini, W. P. Jones, Particle acceleration in turbulent flows: A class of nonlinear stochastic models for intermittency, Phys. Fluids (1994-present) 19 (3) (2007) 035104.

[50] M. Bini, W. P. Jones, Large eddy simulation of an evaporating acetone spray, Int. J. Heat Fluid Flow 30 (3) (2009) 471–480.

[51] M. C. Yuen, L. W. Chen, On drag of evaporating liquid droplets, Combust. Sci. Technol. 14 (4-6) (1976) 147–154.

[52] A. B. Liu, D. Mather, R. D. Reitz, Modelling the effects of drop drag and breakup on fuel sprays, SAE Technical Paper (1993).

[53] B. Abramzon, W. A. Sirignano, Droplet vaporisation model for spray combustion calculations, Int. J. Heat Mass Transfer 32 (9) (1989) 1605–1618.

[54] W. E. Ranz, W. R. Marshall, Evaporation from drops: Part I, Chem. Engng. Prog 48 (1952) 141–146.

[55] W. E. Ranz, W. R. Marshall, Evaporation from drops: Part II, Chem. Engng. Prog 48 (1952) 173–180.

[56] L. Crocco, Theoretical studies on liquid-propellant rocket instability, Symp. (Int.) Combust. 10 (1965) 1101–1128.

[57] R. Clift, J. R. Grace, M. E. Weber, Bubbles, drops, and particles, Courier Corporation, 2005.

[58] B. Abramzon, S. Sazhin, Convective vaporisation of a fuel droplet with thermal radiation absorption, Fuel 85 (1) (2006) 32–46.

[59] X.-Q. Chen, J. C. F. Pereira, Computation of turbulent evaporating sprays with well-specified measurements: a sensitivity study on droplet properties, Int. J. Heat Mass Transfer 39 (3) (1996) 441–454.

[60] R. S. Miller, K. Harstad, J. Bellan, Evaluation of equilibrium and non-equilibrium evaporation models for many-droplet gas-liquid flow simulations, Int. J. Multiphase Flow 24 (6) (1998) 1025–1055.

[61] G. L. Hubbard, V. E. Denny, A. F. Mills, Droplet evaporation: effects of transients and variable properties, Int. J. Heat Mass Transfer 18 (9) (1975) 1003–1008.

[62] A. Burcat, B. Ruscic, Third millenium ideal gas and condensed phase thermochemical database for combustion with updates from active thermochemical tables, Argonne National Laboratory Argonne, IL, 2005.

[63] T. H. Chung, L. L. Lee, K. E. Starling, Applications of kinetic gas theories and multiparameter correlation for prediction of dilute gas viscosity and thermal conductivity, Ind. Eng. Chem. Fundam. 23 (1) (1984) 8–13.

[64] T. H. Chung, M. Ajlan, L. L. Lee, K. E. Starling, Generalised multiparameter correlation for nonpolar and polar fluid transport properties, Ind. Eng. Chem. Res. 27 (4) (1988) 671–679.

[65] S. Chapman, T. G. Cowling, The mathematical theory of non-uniform gases: an account of the kinetic theory of viscosity, thermal conduction and diffusion in gases, Cambridge university press, 1970.

[66] C. R. Wilke, A viscosity equation for gas mixtures, J. Chem. Phys. 18 (4) (1950) 517–519.

[67] C. R. Wilke, Diffusional properties of multicomponent gases, Chem. Eng. Prog. 46 (2) (1950) 95–104.

[68] A. Wassiljewa, Wärmeleitung in gasgemischen, Phys. Z 5 (22) (1904) 737.

[69] J. C. Lasheras, C. Eastwood, C. Martínez-Bazán, J. Montanes, A review of statistical models for the break-up of an immiscible fluid immersed into a fully developed turbulent flow, Int. J. Multiphase Flow 28 (2) (2002) 247–278.

[70] G. K. Batchelor, The theory of homogeneous turbulence, Cambridge university press, 1953.

[71] C. Martínez-Bazán, J. L. Montañés, J. C. Lasheras, On the breakup of an air bubble injected into a fully developed turbulent flow. Part 1. Breakup frequency, J. Fluid Mech. 401 (1999) 157–182.

[72] C. D. Eastwood, A. Cartellier, J. C. Lasheras, The breakup time of a droplet in a fully-developed turbulent flow, in: APS Division of Fluid Dynamics Meeting Abstracts, Vol. 1, 1999.

[73] J. C. Lasheras, E. Villermaux, E. J. Hopfinger, Break-up and atomisation of a round water jet by a high-speed annular air jet, J. Fluid Mech. 357 (1998) 351–379.

[74] J. C. Lasheras, E. J. Hopfinger, Liquid jet instability and atomisation in a coaxial gas stream, Annu. Rev. Fluid Mech. 32 (1) (2000) 275–308.

[75] C. Martínez-Bazán, J. L. Montañés, J. C. Lasheras, On the breakup of an air bubble injected into a fully developed turbulent flow. Part 2. Size PDF of the resulting daughter bubbles, J. Fluid Mech. 401 (1999) 183–207.

[76] C. Martínez-Bazán, J. Rodríguez-Rodríguez, G. B. Deane, J. L. Montañés, J. C. Lasheras, Considerations on bubble fragmentation models, J. Fluid Mech. 661 (2010) 159–177.

[77] V. G. McDonell, G. S. Samuelsen, An experimental data base for the computational fluid dynamics of reacting and nonreacting methanol sprays, J. Fluids Eng. 117 (1) (1995) 145–153.

[78] M. Klein, A. Sadiki, J. Janicka, A digital filter based generation of inflow data for spatially developing direct numerical or large eddy simulations, J. Comput. Phys. 186 (2) (2003) 652–665.

[79] T. Marchione, C. Allouis, A. Amoresano, F. Beretta, Experimental investigation of a pressure swirl atomiser spray, J. Propul. Power 23 (5) (2007) 1096–1101.

[80] P. Kloeden, E. Platen, Numerical Solution of Stochastic Differential Equations, Springer Berlin Heidelberg, 2013.

[81] J. Li, Z. Zhao, A. Kazakov, M. Chaos, F. L. Dryer, J. J. Scire, A comprehensive kinetic mechanism for CO, CH2O, and CH3OH combustion, Int. J. Chem. Kinet. 39 (3) (2007) 109–136.

[82] T. J. Held, F. L. Dryer, A comprehensive mechanism for methanol oxidation, Int. J. Chem. Kinet. 30 (11) (1998) 805–830.

[83] S. Gallot Lavallée, W. P. Jones, A. J. Marquis, Large Eddy Simulation of an Ethanol Spray Flame Under MILD Combustion with the Stochastic Fields Method, Proc. Combust. Inst. 36, to appear.

[84] V. G. McDonell, M. Adachi, G. S. Samuelsen, Structure of reacting and non-reacting swirling air-assisted sprays, Combust. Sci. Technol. 82 (1-6) (1992) 225–248.

[85] K. D. Squires, J. K. Eaton, Particle response and turbulence modification in isotropic turbulence, Phys. Fluids A: Fluid Dynamics (1989-1993) 2 (7) (1990) 1191–1203.

[86] S. K. Marley, E. J. Welle, K. M. Lyons, W. L. Roberts, Effects of leading edge entrainment on the double flame structure in lifted ethanol spray flames, Exp. Therm Fluid Sci. 29 (1) (2004) 23–31.

[87] S. K. Marley, K. M. Lyons, K. A. Watson, Leading-edge reaction zones in lifted-jet gas and spray flames, Flow Turbul. Combust. 72 (1) (2004) 29–47.

[88] M. S. Mansour, I. Alkhesho, S. H. Chung, Stabilization and structure of n-heptane flame on CWJ-spray burner with kHZ SPIV and OH-PLIF, Exp. Therm Fluid Sci. 73 (2016) 18–26.

[89] N. Peters, Turbulent Combustion, Cambridge University Press, New York, 2000.

[90] M. A. Tanoff, M. D. Smooke, R. J. Osborne, T. M. Brown, R. W. Pit, The sensitive structure of partially premixed methane-air vs. air counterflow flames, Symp. (Int.) Combust. 26 (1996) 1121–1128.

[91] J. B. Kelman, A. R. Masri, Simultaneous imaging of temperature and OH number density in turbulent diffusion flames, Combust. Sci. Technol. 122 (1-6) (1997) 1–32.

[92] F. Shum-Kivan, J. M. Santiago, A. Verdier, E. Riber, B. Renou, G. Cabot, B. Cuenot, Experimental and numerical analysis of a turbulent spray flame structure, Proc. Combust. Inst. 36 (2) (2017) 2567–2575.